

Recent Precipitation Decrease Across the Western Greenland Ice Sheet Percolation Zone

Lewis, Gabriel¹; Osterberg, Erich¹; Hawley, Robert¹; Marshall, Hans Peter²; Meehan, Tate²; Graeter, Karina³; McCarthy, Forrest⁴; Overly, Thomas^{5,6}; Thundercloud, Zayta¹; Ferris, David¹

¹Department of Earth Sciences, Dartmouth College, Hanover, NH, USA

²Geosciences Department, Boise State University, Boise, ID, USA

³Office of Sustainability, University of Maine, Orono, ME, USA

⁴College of Fisheries and Ocean Sciences, University of Alaska Fairbanks, Fairbanks, AK, USA

⁵NASA Cryospheric Sciences Laboratory, NASA Goddard Space Flight Center, Greenbelt, MD, USA

⁶Earth System Science Interdisciplinary Center (ESSIC), University of Maryland, College Park, MD, USA

Correspondence to: Gabriel Lewis (Gabriel.M.Lewis.GR@dartmouth.edu)

Abstract

The mass balance of the Greenland Ice Sheet (GrIS) in a warming climate is of critical interest in the context of future sea-level rise. Increased melting in the GrIS percolation zone due to atmospheric warming over the past several decades has led to increased mass loss at lower elevations. Previous studies have hypothesized that this warming is accompanied by a precipitation increase, as would be expected from the Clausius-Clapeyron relationship, compensating for some of the melt-induced mass loss throughout the Western GrIS. This study tests that hypothesis by calculating snow accumulation rates and trends across the Western GrIS percolation zone, providing new critical accumulation estimates in regions with sparse *in situ* data or data that does not span the recent accelerating surface melt. We present accumulation records from sixteen 22 – 32 m long firn cores and 4436 km of ground penetrating-radar, covering the past 20 – 60 years of accumulation, collected across the Western GrIS percolation zone as part of the Greenland Traverse for Accumulation and Climate Studies (GreenTrACS) project. Trends from both radar and firn cores, as well as commonly used regional climate models, show decreasing accumulation and precipitation of $2.4 \pm 1.5 \% \text{ a}^{-1}$ over the 1996 – 2016 period, which we attribute to shifting storm-tracks related to stronger atmospheric summer blocking over Greenland. Changes in atmospheric circulation over the past 20 years, specifically anomalously high summertime blocking, have reduced GrIS surface mass balance through both an increase in surface melting and a decrease in accumulation.

1. Introduction

Greenland Ice Sheet (GrIS) mass loss has accelerated over the past few decades, with modern mass loss rates more than double those from Antarctica (van den Broeke et al., 2016). The 2010-2018 GrIS mass loss was calculated as $286 \pm 20 \text{ Gt a}^{-1}$ (Mouginot et al., 2019), contributing $0.7 \pm 0.2 \text{ mm a}^{-1}$ of sea level rise. Over the past 20 years, the largest warming rates (Hanna et al., 2012) and fastest mass loss have occurred in Western

34 Greenland (26 ± 7 GT a⁻² in basins F + G of Sasgen et al., 2012). Here, regional scale models calculate a
35 surface mass balance (SMB) decrease ranging from 31.1% (European Centre for Medium Range Weather
36 Forecasting downscaled; ECMWFd) to 76.5% (Modèle Atmosphérique Régional; MAR) over the 1996 –
37 2008 period (Vernon et al., 2013) as a result of higher surface melt and runoff (van den Broeke et al., 2009,
38 2016). Modern surface melt rates are at their highest levels of at least the last 450 years across Western
39 Greenland (Graeter et al., 2018) and more broadly throughout Greenland (Trusel et al., 2018). In particular,
40 ice core records from Western Greenland show an abrupt increase in surface melt rates beginning in the
41 middle-late 1990's due to a combination of higher North Atlantic sea surface temperatures, enhanced
42 summertime blocking highs, and anthropogenic warming (Graeter et al., 2018).

43
44 Enhanced GrIS surface melt is driven fundamentally by rising Greenland summer temperature trends
45 upwards of 0.135 ± 0.047 °C a⁻¹ from 1982 – 2011 (Hall et al., 2013; Reeves Eyre and Zeng, 2017). Basic
46 physics implies that rising temperatures should cause an increase in accumulation over the ice sheet due to
47 the Clausius-Clapeyron relationship – warmer air has a higher saturation vapor pressure, potentially leading
48 to more precipitation (Box et al., 2006; Buchardt et al., 2012). The Coupled Model Intercomparison Project,
49 phase 5 (CMIP5) predicts precipitation increases of 20 – 50% over the GrIS by the end of the 21st century
50 (Bintanja and Selten, 2014), partially offsetting mass loss and sea-level rise from enhanced summer melt and
51 runoff. However, most *in situ* records of Greenland snow accumulation do not span the modern period of
52 rapid warming since the mid-1990s, making it difficult to determine whether accumulation has been
53 increasing with warming temperatures as predicted. For example, the Program for Arctic Regional Climate
54 Assessment (PARCA) campaign collected accumulation data from a network of 49 ice and firn cores in 1997-
55 1998 (Mosley-Thompson et al., 2001), just at the onset of accelerated surface melting (Graeter et al., 2018).
56 There have been no published *in situ* accumulation records from the Western GrIS percolation zone for the
57 past decade. Updated *in situ* snow accumulation data are needed from this region to assess recent changes in
58 accumulation during this period of warming and SMB loss from melt and runoff.

59
60 In addition to measuring snow accumulation with ice cores and automated snow depth sensors, several studies
61 have used ground-based and airborne radar to calculate GrIS accumulation rates and trends (e.g. Medley et
62 al., 2013; Spikes et al., 2004; Hawley et al., 2014; Koenig et al., 2016). We build upon these previous studies
63 by collecting GPR data across the lower percolation zone of Western Greenland, where airborne radargrams
64 are often obscured by refrozen melt percolation (Nghiem et al., 2005). The *in situ* GPR used in this study
65 operates using a UHF pulsed radar, while other systems such as frequency modulated continuous wave
66 (FMCW) radars use phase-sensitive antennas that include both amplitude and phase information. By having

67 our GPR antenna coupled with the snow, we avoid losing energy, and, therefore, penetration depth, from a
68 strong reflection off of the snow-air interface.

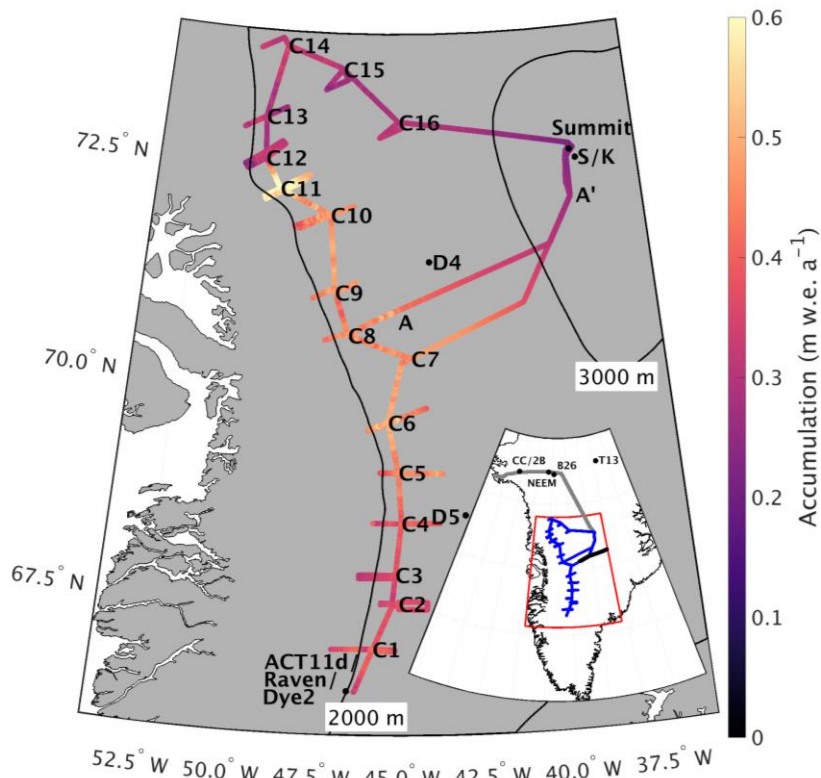
69

70 In addition to temperature-precipitation relationships through the Clausius-Clapeyron relationship, previous
71 studies have analyzed the dynamic climate controls on Greenland precipitation. Mernild et al. (2014), Auger
72 et al. (2017), and Lewis et al. (2017) have hypothesized that a positive Atlantic Multidecadal Oscillation
73 (AMO) index correlates with rising accumulation over most of the GrIS interior, since higher sea surface
74 temperatures increase moisture flux over the GrIS and induce greater snowfall. In addition, high pressure
75 (blocking) systems east of Greenland tend to deflect eastward-moving storms over central Greenland and
76 increase precipitation, whereas blocking directly over Greenland or in Baffin Bay has the potential to reduce
77 accumulation over the GrIS by displacing the polar jet stream and corresponding storm tracks equatorward
78 (Auger et al., 2017). Over the 1991 – 2015 period there has been particularly strong summertime Greenland
79 blocking (Hanna et al., 2016), but its effects on GrIS accumulation have not been determined with *in situ*
80 data.

81

82 Here we develop new accumulation records across the Western GrIS percolation zone using sixteen firn cores
83 and 4436 km of GPR data collected during an over-ice traverse spanning two field seasons. We evaluate the
84 veracity of the accumulation data through comparisons of our firn core time series with previous
85 measurements. We quantify multi-year trends in accumulation across Western Greenland to test the
86 hypothesis that precipitation has recently increased from the Clausius-Clapeyron relationship and higher GrIS
87 temperatures. Further, we assess the ability of RCMs to capture the year-to-year variability and multi-year
88 trends in Western GrIS accumulation. Finally, we evaluate relationships between recent accumulation trends
89 and atmospheric circulation patterns, particularly changes in storm tracks.

90



91

92

93

94

95

Figure 1. Average accumulation across the GreenTrACS traverse for the length of each record showing the location of each firn core, ACT11d, D4, D5, Katie (K), Raven/Dye-2, and Sandy (S) ice cores, and Summit Station. Transect A-A' discussed in Section 3.3. Inset shows locations of Camp Century (CC), 2Barrel (2B), NEEM, B26, and TUNU2013 (T13) ice cores, as well as locations of EGIG (black), GrIT (grey), and GreenTrACS (blue) traverses.

96

2. Methods

97

98

99

100

101

102

103

104

105

106

107

108

This study uses data from the 2016 – 2017 Greenland Traverse for Accumulation and Climate Studies (GreenTrACS), which measured accumulation and melt across the Western GrIS percolation zone over two summer snowmobile traverses (closely following the 2150 m a.s.l. elevation contour). The May – June 2016 season traversed 860 km from Raven/Dye-2 northward to Summit Station, while the May – June 2017 traverse made a 1230 km clockwise loop starting and ending at Summit Station (**Error! Reference source not found.**Figure 1). This manuscript focuses on accumulation rates derived from 400 MHz GPR data collected along the entire traverse path, as well as sixteen shallow (22 – 32 m deep) firn cores spaced 40 – 100 km apart along the backbone of the traverse (Figure 1). Firn Cores 1 – 7 were collected in 2016 and Cores 8 – 16 were collected in 2017. We returned to the Core 7 location at the beginning of the 2017 traverse to recover a weather station and to connect the two season’s GPR data. Additionally, we collected GPR data ~30 – 70 km east and west of each core site, hereafter called “spurs”, to measure changes in accumulation along strong elevation gradients (see Figure 1).

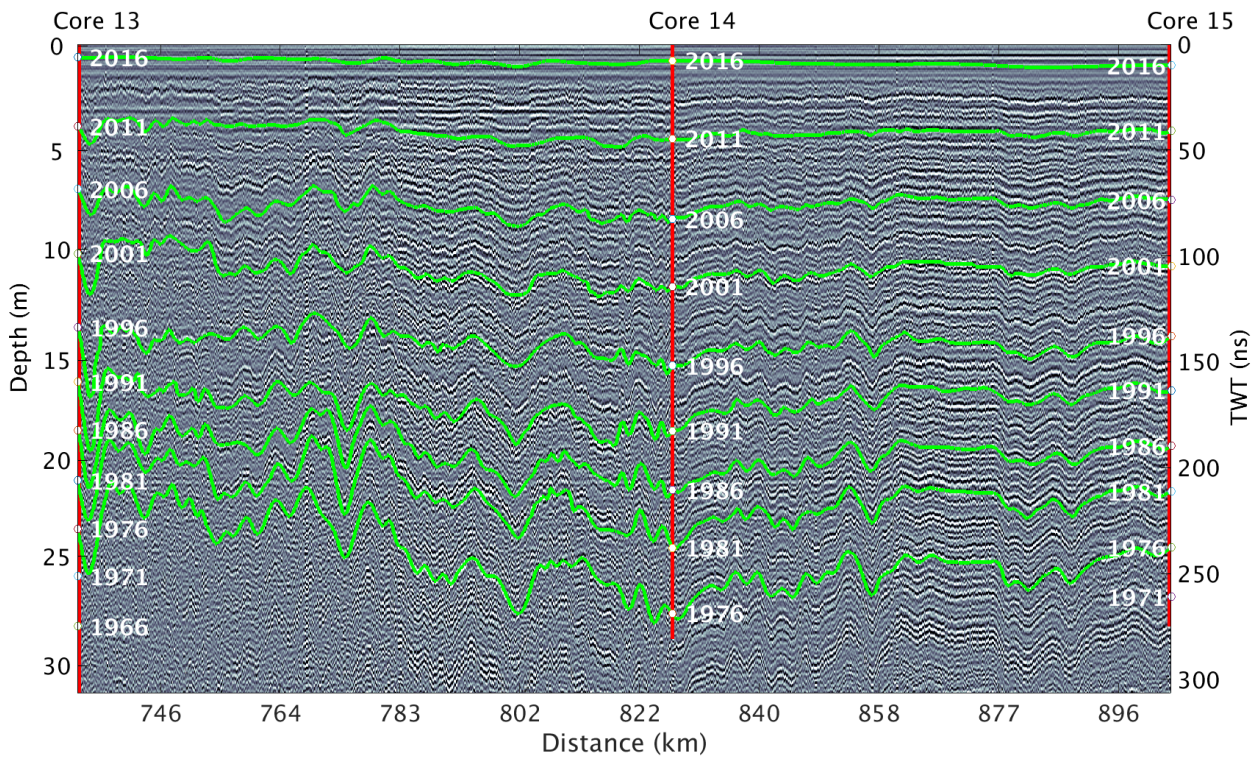
2.1. GPS Positioning

During the 2016 traverse we collected GPS data using a Trimble NetR8 reference receiver with a Zephyr Geodetic antenna mounted to a Nansen sled ~5 m in front of the GPR antenna. For each spur and the tail ends of each transect between core sites we performed differential corrections to the GPS data using RTKLIB 2.4.1 and a Trimble NetR8 base station near the core site. Between spurs, when not operating a base station, we post-processed GPS data in precise point positioning mode (Zumberge et al., 1997). Estimated root-mean-square horizontal errors were generally between 13 and 18 cm from standard deviations calculated during stationary periods at the end of spurs. To co-register GPR and GPS data, we used time stamps embedded in the two data streams and locations where we stopped to save GPR files, approximately every 15 km. The time drift in the GPR logger is negligible over these durations.

During the 2017 traverse we used GPS data from a Garmin 19x GPS receiver wired directly to the GPR instrument, which recorded position data at every radar sample with RMS values of 3 m. During radar processing we average 75 adjacent traces, corresponding to a distance of ~20 m, so errors in GPS positioning have a negligible effect on the final dataset.

2.2. Ground-penetrating radar

We develop a spatially continuous record of accumulation using GPR profiles collected with Geophysical Survey Systems Inc. (GSSI) SIR-3000 (during 2016) and SIR-30 (during 2017) radar units with a 400 MHz antenna (following Hawley et al., 2014). The antenna was towed on the snow surface in a small plastic sled ~5 m behind a wooden Nansen sled and ~15 m behind a snow machine. We recorded 2048 samples (2016) and 4096 samples (2017) per trace over a range window of 800 ns (Figure 2). The 400 MHz short-pulse radar has a range resolution (ability to resolve distinct features) of 0.35 ± 0.1 m in firn, which is fine enough to resolve Internal Reflecting Horizons (IRHs) that have been shown to represent isochrones (Medley et al., 2013; Rodriguez-Morales et al., 2014; Spikes et al., 2004; Hawley et al., 2014). We recorded 10 traces per second, which at the snowmobile's average travel speed of approximately 2.75 m s^{-1} results in ~3.6 traces recorded per meter. Note that this spacing between traces varies with vehicle speed.



136
137
138
139
140

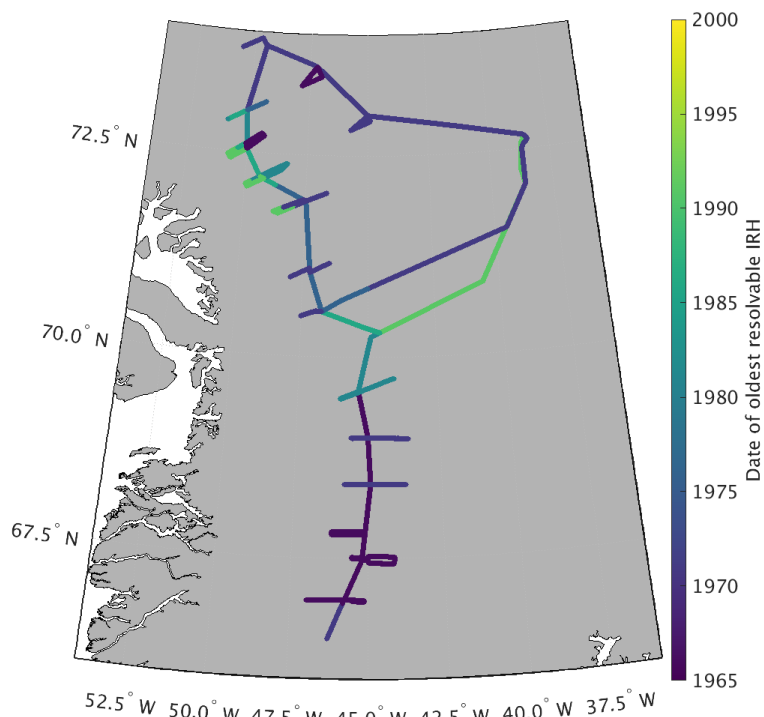
Figure 2. Radargram showing the top 32 m of the transect along the main 2017 traverse from Core 13 to Core 15. Cores are indicated as red lines down to their final depth, with dates plotted every 5 years at corresponding depths. Traced internal reflecting horizons are shown as isochronous green lines. The depth scale on the vertical axis is calculated from the TWT-depth conversion (see Section 2.4) for Core 13, although there is no visual difference in depth scale across this radargram.

141 Depending on signal attenuation within the firn column, IRHs can be traced to a depth of 20 – 50 m (Figure
142 2), providing accumulation records over the past 20 – 60 years (Figure 3). For areas with high attenuation
143 (i.e. shallow penetration of the radar signal), such as lower elevation regions with more refrozen melt layers,
144 we calculate accumulation results for shorter time periods. We are not able to trace as many IRHs to the west
145 of Cores 10 – 13 compared to the east due to higher signal attenuation, resulting in slightly different (less
146 than $0.03 \text{ m w.e a}^{-1}$) average accumulation values on either side of these core locations (Figure 3). Likewise,
147 we experienced an equipment malfunction at the end of the 2016 traverse, reducing the number of observable
148 IRHs from Core 7 to Summit Station (Figure 3). We have less confidence in calculated accumulation
149 throughout this section of the traverse due to this malfunction, although the 2017 Summit to Core 8 interval
150 overlaps nicely with the last 140 km of the problematic 2016 interval, and provides high quality accumulation
151 measurements for this section near Summit Station.

152

153 We reduce the GPR data volume and signal noise by averaging 75 adjacent traces, which has the effect of
154 suppressing random noise by the principle of trace stacking (Yilmaz, 2001). We apply a combination of
155 median trace filtering, residual mean filtering (Gerlitz et al., 1993), and bandpass filtering using a butterworth
156 design (Selesnick and Sidney Burrus, 1998) between 200 – 800 MHz. For data visualization, we apply an
157 automatic gain control (Yilmaz, 2001) to give the interpreter more confidence when picking IRHs.

158
159



160
161
162

Figure 3: Date of oldest resolvable internal reflecting horizon throughout the entire GreenTrACS traverse route. Anomalously young ages from Core 7 to Summit are due to equipment malfunction.

163

164 2.3. Firn core processing and density profiles

165 The amount of snow mass and the time span between IRHs are necessary to calculate accumulation rates
166 from the GPR profiles. The accumulation rate is a function of the depth-age scale, travel time-depth
167 conversion rate, and the firn density profile. We obtain the depth-age and depth-density scales from each of
168 the shallow firn cores collected along the GreenTrACS traverse, and from density models based on
169 temperature and accumulation rate data.

170

171 The sixteen firn cores were drilled using an Ice Drilling Program hand auger with a Kyne sidewinder
172 attachment (see Graeter et al., 2018). We sampled the firn cores for chemical measurements using a
173 continuous ice core melter system with discrete sampling (Osterberg et al., 2006). We used an Abakus (Klotz)
174 laser particle detector to measure microparticle concentrations and size distribution from the continuous ice
175 core meltwater stream, a Dionex Model ICS5000 capillary ion chromatograph to measure major ion (Na^+ ,
176 Mg^{2+} , Ca^{2+} , K^+ , NH_4^+ , Cl^- , NO_3^- , SO_4^{2-}) and methanesulfonic acid concentrations, and a Picarro L1102-I and

177 a Los Gatos Research Liquid Water Isotope Analyzer to measure oxygen and hydrogen isotope ratios ($\delta^{18}\text{O}$,
178 δD ; Graeter et al., 2018).

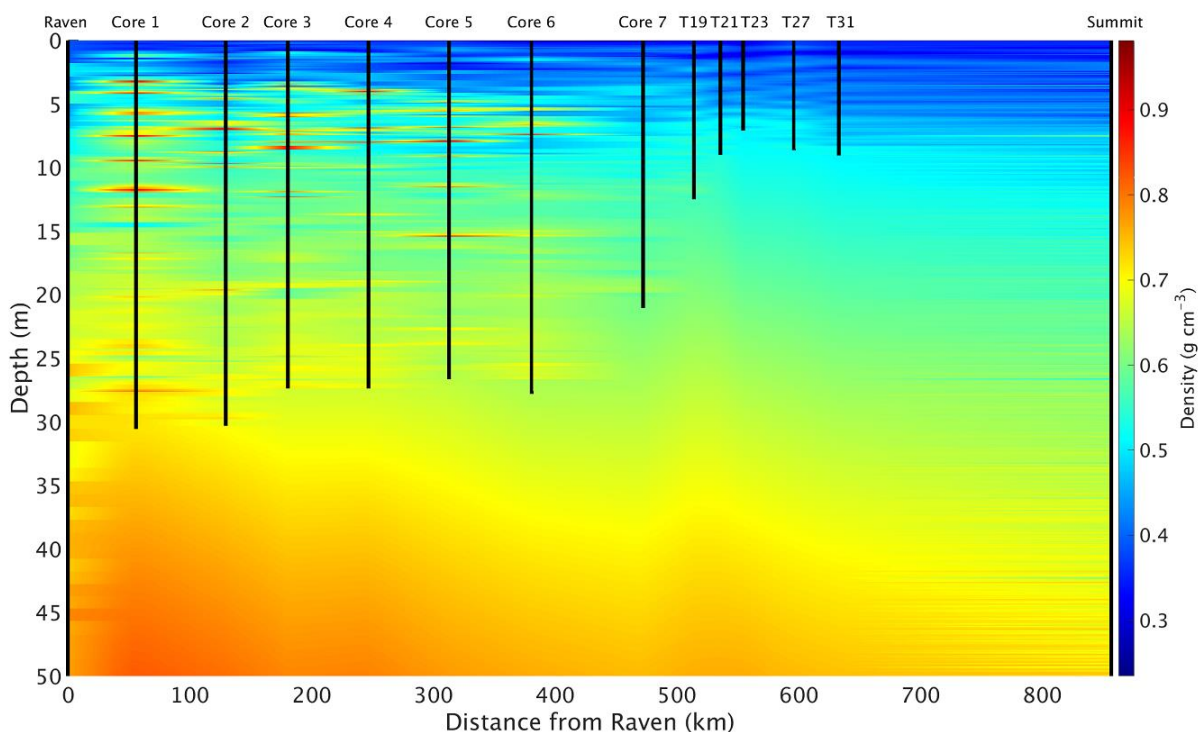
179
202 We determine depth-age curves for each core by identifying annual layers based on seasonal oscillations in
203 $\delta^{18}\text{O}$ and the concentrations of major ions and dust, consistent with previous ice core studies in this region
204 (Graeter et al., 2018; Mosley-Thompson et al., 2001; Osterberg et al., 2015). While meltwater percolation
205 smooths the signal of some of these tracers, we can still confidently determine the depth-age curve using
206 nearly unperturbed oscillations in $\delta^{18}\text{O}$ and dust. We combine the depth-age scales with measured density to
207 calculate annual accumulation rates at the firn core sites.

208
209 At each firn core and at the ends of each spur, we measured the density in the top meter of snow using a 1000
210 cm^3 SnowMetrics cutter. To calculate density profiles from the firn cores, we measured the mass, length, and
211 diameter of 0.03–1 m long core segments in the field and again after transporting the cores to the Dartmouth
212 College Ice Core Laboratory. Additionally, we measured melt layer thickness in the laboratory following
213 Graeter et al. (2018). To calculate accumulation rates at Raven/Dye-2, we use density data from a 119.6 m
214 long firn core collected in 1997 (Bales et al., 2009) and a 19.3 m long core collected from the same location
215 in 2015, which did not include accumulation data (Vandecrux et al., 2018). For this location we use the most
216 recent density data for the near-surface and the older densities for depths below the 2015 core. Likewise, we
217 use a density profile from a 109 m long firn core collected from Summit in 2010 (Mary Albert, personal
218 communication, 2015). We also incorporate density data from measurements along the EGIG traverse at T19,
219 T21, T23, T27, and T31 to improve the density profile between Core 7 and Summit (Morris and Wingham,
220 2014).

221
222 After collecting each firn core, we measured borehole temperature for 24 – 48 hours using a 20 m long
223 thermistor string. We estimate mean annual temperature from the deepest thermistor on the twenty-
224 thermistor-string. These measurements agree with MODIS satellite derived mean annual temperature (Hall
225 et al., 2012) to within ± 1 °C for each firn core location. For the location of each firn core, we use the depth-
226 density data from that core and calculate a Herron and Langway (1980) depth-density model for depths below
227 the core using our measured mean annual temperature, firn core mean annual accumulation, and top-meter
228 snow density. Likewise, we calculate Herron-Langway profiles for the ends of each spur using MODIS
229 satellite derived mean annual temperature (Hall et al., 2012), MAR modeled accumulation (Burgess et al.,
230 2010), and the measured snow density in the upper meter of each of the spur’s snow pits. Finally, we
231 interpolate depth-density profiles both between firn cores and along radar spurs to estimate the depth-density

232 matrix everywhere along our traverse (Figure 4). Final calculated accumulation rates are insensitive to the
233 input accumulation parameter we use to calculate our Herron-Langway models (Lewis et al., 2017).

234
235 As shown in Figure 4, ice layers within several firn cores are extrapolated laterally along the traverse,
236 although these dense lenses are typically both localized and heterogeneous at these elevations (Brown et al.,
237 2011; Rennermalm et al., 2013). Numerous studies have documented the heterogeneity of firn throughout
238 the percolation zone and the complications of calculating SMB due to ice pipes and lenses (Brown et al.,
239 2011, 2012; De La Peña et al., 2015). Here we attempt to accurately calculate accumulation using interpolated
240 firn cores and *in situ* GPR throughout this complicated region. Our ice lens density interpolation is as accurate
241 as possible between firn cores without additional *in situ* data, and this estimation does not significantly alter
242 our results, as discussed in Section 2.6, since the ice layers represent a small fraction of the total depth to
243 IRHs.



244
245 **Figure 4. Depth-density profile along the main 2016 traverse used for calculation of electromagnetic wave velocity and accumulation in**
246 **this study. Densities are linearly interpolated between the two nearest cores and are modeled using Herron-Langway profiles below the**
247 **depth of each core. The left and right boundary data come from the Raven/Dye-2 and Summit firn cores, respectively. Ice layers in Cores**
248 **1 – 5 are clearly visible as red lenses, but their extent is, in reality, likely more localized.**

249 250 **2.4. Travel-time to depth conversion**

251 We convert the radar travel time to depth by iteratively multiplying the velocity of the electromagnetic wave
252 by the signal's one-way travel time to each IRH. The electromagnetic speed of the radar wave, v (m s^{-1}), is

253 calculated from the relative dielectric permittivity, ϵ_r (dimensionless), and the speed of light in a vacuum, c
254 ($3 \times 10^8 \text{ m s}^{-1}$), from
255 $v = \frac{c}{\sqrt{\epsilon_r}}$ (1).

256 In turn, we calculate the relative dielectric permittivity from the density, ρ (g cm^{-3}), of snow and ice at depth,
257 as shown in Figure 4, for each radar trace at every range bin (following Kovacs et al., 1995) by
258 $\epsilon_r = (1.0 + 0.845 * \rho)^2$ (2).

259 We calculate the depth of each subsequent radar sample for each trace in the profile using the radar travel
260 time and velocity profile from equations 1 and 2, following Hawley et al. (2014) and Lewis et al. (2017).

261

262 **2.5. Internal reflecting horizons**

263 We manually select 10 clear, strong IRHs spaced approximately 5 years apart to consistently trace from
264 Raven/Dye-2 to Summit Station and throughout the 2017 main traverse (Figure 2). We trace each layer
265 manually by visually identifying strong amplitude peaks throughout the radargram, starting with the 2016
266 layer and working downwards. We use a spline interpolation between manual picks to trace each layer along
267 large amplitude reflections every $\sim 500 - 700 \text{ m}$ along the traverse. When a layer appears to bifurcate due to
268 changes in accumulation, we continue to trace the layer based on the trajectory of surrounding IRHs. Each
269 horizon is traced throughout the traverse, except in areas where the attenuated signal makes it too difficult to
270 interpret (Figure 3). We trace layers for each spur starting at the depth of each layer at the corresponding firn
271 core location. We can trace layers below the depth of some firn cores by tracing them from cores that are
272 deeper or have lower accumulation rates.

273

274 We trace layers between cores using a connect-the-dots approach using the depth-age scale at each firn core.
275 We trace layers from one firn core to the next before checking that we intersect that core location at the
276 proper depth for the age of our traced IRH. Note that the depths of several layers at Cores 2 – 16 are located
277 below the bottom depth of those cores. Since these layers are isochronous, they are used to calculate
278 accumulation over appropriate time epochs by using dates obtained from intersections with other cores (see
279 Figure 3).

280

281 **2.6. Accumulation calculations and uncertainty**

282 Finally, we calculate snow accumulation using the firn core depth-age scales, measured and interpolated
283 depth-density profiles (Figure 4), and traced IRHs (Figure 2). We calculate the water equivalent accumulation

284 \dot{b} (m w.e. a⁻¹) between adjacent IRHs from the depth z (m) and age t (year) of each layer, the average density
285 ρ (kg m⁻³) between layers, and the density of water ρ_w (1000 kg m⁻³):

$$286 \quad \dot{b} = \frac{1}{t_2 - t_1} \int_{z_1}^{z_2} \frac{\rho(z)}{\rho_w} dz \quad (3).$$

287
288 We correct for layer thinning using a Nye (1963) model. The thinning factor has an average value of 0.9993
289 \pm 0.0003 and is multiplied by the accumulation rate for each radar trace. For each radar trace, the thinning
290 factor, $\lambda(z)$, is calculated from the average accumulation \dot{b} (m w.e. a⁻¹) of each epoch, average age of the
291 epoch a (year), and water equivalent thickness of the GrIS H (m), from Morlighem et al. (2014):

$$292 \quad \lambda(z) = e^{-\frac{\dot{b}}{H}a} \quad (4).$$

293
294 Accumulation uncertainty can arise from independent errors in tracing IRHs, errors from incorrectly dating
295 firm cores, and/or errors in the densities used for converting from separation distance to water equivalent
296 accumulation. To reduce tracing errors, we retraced each IRH along the two main traverse paths four times
297 apiece. Close inspection of the IRHs reveals that the peaks defining IRHs are within \pm 2 radar samples (within
298 at most \pm 0.12 m), and incorrectly jumping to the next IRH would result in an error of at most \pm 10 samples
299 (within \pm 0.55 m). We chose an epoch between IRHs of 5.0 years from the firm core chemistry depth-age
300 scales, which corresponds to a maximum tracing error of \sim \pm 0.11 m a⁻¹ for each epoch, or a maximum error
301 of \pm 0.061 m w.e a⁻¹ given an average firm density of 0.55 g cm³ across this dataset.

302
303 We perform a leave-one-out cross validation to calculate accumulation errors at locations where we do not
304 have firm core density profiles. Here we choose one of the sixteen firm cores, in addition to the Raven/Dye-2
305 and Summit cores, to omit from our density interpolation (Figure 4), so that we interpolate density profiles
306 between adjacent firm cores and a Herron-Langway profile at the missing core location. We find maximum
307 single-epoch errors of 0.079 m w.e. a⁻¹ and maximum RMS (1971 – 2016) errors of 0.046 m w.e. a⁻¹ (Table
308 1) at the location of missing cores. These differences are approximately twice as large at Cores 1 – 6 than
309 Cores 7 – 16 due to larger differences between measured and interpolated density profiles, likely a result of
310 meltwater percolation and ice lenses (Graeter et al., 2018).

311
312 Similarly, we perform a leave-out-out validation by omitting a firm core density profile location entirely and
313 interpolating density profiles over a larger distance (e.g. between Core 1 and Core 3). In this case we find
314 maximum single-epoch errors of 0.057 m w.e. a⁻¹ and maximum RMS (1971 – 2016) errors of 0.033 m w.e.
315 a⁻¹. Throughout this study, we use our measured density profiles to calculate accumulation at core locations,
316 rather than rely on Herron-Langway density models that would result in larger uncertainties.

317
318
319
320
321
322
323
324
325
326
327
328
329

We conservatively take our accumulation error from missing density measurements to be 0.079 m w.e. a⁻¹. This error highlights the importance of our firn core spacing between 40 – 100 km along the traverse and confirms that the accuracy of future remotely sensed radar accumulation (e.g. IceBridge snow and accumulation radars) estimates depend on precise field-based *in situ* density profiles for accurate accumulation history in the percolation zone. Overly et al. (2016) calculated accumulation in the dry snow zone using Herron-Langway profiles within 3.5% of accumulation calculated using neutron-probe density profiles. However, here we show that *in situ* measurements, or accurate meltwater percolation modeling (Meyer and Hewitt, 2017), are required to correctly calculate SMB in the percolation zone.

Table 1. Difference between accumulation rates at each GreenTrACS core site calculated using Herron-Langway profiles and firn core density information.

Core	RMS average difference (m w.e. a ⁻¹)	Max epoch difference (m w.e. a ⁻¹)	Max Epoch difference (% of acc.)
1	0.046	0.079	20.1
2	0.025	0.061	16.2
3	0.037	0.074	19.9
4	0.028	0.045	10.7
5	0.026	0.054	11.5
6	0.038	0.052	10.0
7	0.015	0.026	5.4
8	0.026	0.045	10.3
9	0.030	0.049	10.9
10	0.019	0.039	8.5
11	0.023	0.035	5.0
12	0.018	0.027	8.2
13	0.025	0.031	10.7
14	0.019	0.027	8.2
15	0.010	0.016	5.3
16	0.014	0.025	8.2

330
331
332
333
334
335

We assume uncertainty in dating the firn cores from annual variations in chemistry to be ±0.5 years (Buchardt et al., 2012). At the lowest accumulation locations, the smallest distance between layers is 0.15 m w.e. over an epoch of 4.91 years. This gives an uncertainty in accumulation due to dating of at most ~±0.03 m w.e. a⁻¹. The error associated with measuring *in situ* firn density has been estimated to be 1.4% (Karlöf et al., 2005). However, following Hawley et al. (2014) and Lewis et al. (2017), we conservatively assume that our

336 measurements have a density measurement error of up to twice this large, corresponding to a maximum
337 accumulation error of ± 0.014 m w.e. a^{-1} .

338
339 We calculate the total uncertainty from formal error propagation (following Bevington and Robinson, 1992)
340 from the average accumulation rate $\dot{b} = 0.385$ m w.e. a^{-1} , average thickness between IRHs $\Delta h = 3.56$,
341 uncertainty in tracing δh , average firm density ρ , uncertainty in density measurements $\delta\rho$, average time
342 period between IRHs Δt , and uncertainty in core dating δt . We find the total accumulation rate uncertainty
343 for each epoch to be 0.0709 m w.e. a^{-1} from equation 5.

$$344 \sigma_{epoch} = \sqrt{\dot{b}^2 \left(\left(\frac{\delta h}{\Delta h} \right)^2 + \left(\frac{\delta t}{\Delta t} \right)^2 + \left(\frac{\delta \rho}{\rho} \right)^2 \right)} \quad (5)$$

345
346 Due to the random and non-systematic nature of these errors, we can assume that they are unlikely to
347 contribute to a regional or temporal accumulation bias. To calculate uncertainty for accumulation averaged
348 over multiple epochs ($\sigma_{n-epochs}$) we divide our uncertainty σ_{epoch} by the square root of the number of traced
349 layers (n) at that location.

$$350 \sigma_{n-epochs} = \frac{\sigma_{epoch}}{\sqrt{n}} \quad (6).$$

351

352 **2.7. Model comparison**

353 We compare our GreenTrACS accumulation results with annual outputs from Box et al. (2013; hereafter
354 “Box13”; 1840 – 1999), the Fifth Generation Mesoscale Model (Polar MM5; 1958 – 2008; Burgess et al.,
355 2010), MAR (1948 – 2015; Fettweis et al., 2016), and the Regional Atmospheric Climate Model (RACMO2;
356 1958 – 2015; Noël et al., 2018) over common time periods. Grid cell sizes for these model outputs are 5 km,
357 3 km, 5 km, and 1 km, respectively. For each radar trace we calculate statistically significant differences (at
358 $\alpha = 0.05$) using a two sample t-test with the GreenTrACS accumulation records for each epoch and RCM
359 accumulation for each common year. Additionally, we compare our GreenTrACS accumulation with an
360 accumulation map kriged from 295 firm cores and 20 coastal weather stations (Bales et al., 2009; hereafter
361 “Bales09”). We perform the same two sample t-test with the reported Bales09 uncertainty of 0.092 m w.e. a^{-1}
362 (Bales et al., 2009).

363

364 **2.8. Accumulation trends**

365 To investigate recent changes in GrIS accumulation, we calculate trends in accumulation across our GPR and
366 GreenTrACS firm core dataset. We fit a linear model to the accumulation time series for each radar trace and

367 analyze the trend for both slope and statistical significance. Likewise, we calculate trends and their statistical
368 significance for total precipitation (snowfall + rainfall) for MAR and RACMO2 grid cells from 1996 through
369 the end of both models' temporal coverage. We can compare these results with our accumulation trends since
370 precipitation and accumulation are nearly identical above the equilibrium line altitude, due to zero runoff and
371 negligible sublimation within the percolation zone.

372 **2.9. Storm track changes**

373 To investigate the potential role of changing storm tracks in precipitation changes over the Western GrIS, we
374 utilize the updated Serreze (2009) storm track database. This database contains six-hour interval positions of
375 extratropical cyclone storm centers on a 2.5° grid. These centers are defined when a gridpoint sea level
376 pressure is surrounded by gridpoints at least 2 mb higher than the central point (Serreze, 2009). We calculate
377 the total number of days in which a storm center is located within our region of interest for each season. To
378 determine statistical significance, we run a two sample t-test on the number of storms in our region of interest
379 between 1958 – 1996 compared with 1996 – 2016.

380 **3. Results and discussion**

381 **3.1. Firn core and GPR accumulation records**

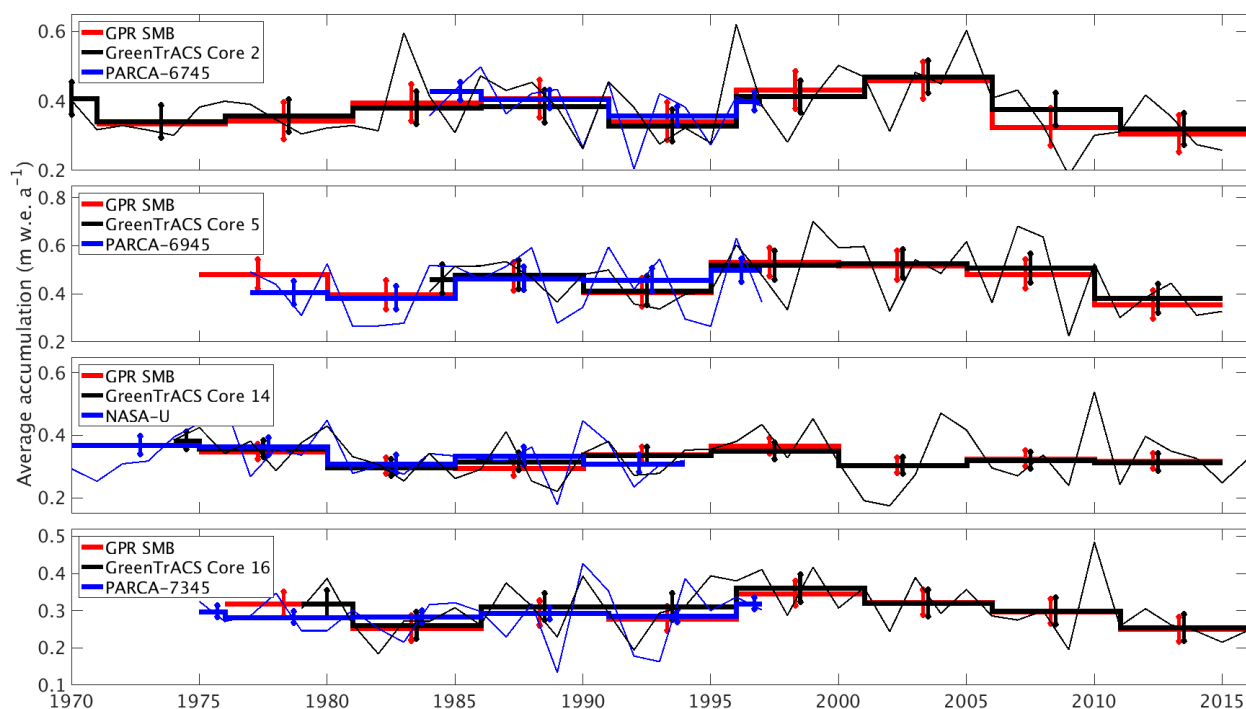
382 Figure 1 displays the mean accumulation at each location along the traverse route, with higher accumulation
383 rates in the southwest and lower accumulation rates at higher elevations of the ice sheet interior, broadly
384 consistent with previously published accumulation compilations (e.g. Bales et al., 2009) and RCM output
385 (Box et al., 2013; Burgess et al., 2010; Fettweis et al., 2016; Noël et al., 2018). We analyze localized
386 differences between GPR derived accumulation and these RCMs in Section 3.3. There is an especially high
387 accumulation zone near Core 11 (0.685 m w.e. a⁻¹), nearly double the accumulation at Core 10 (0.453 m w.e.
388 a⁻¹) and Core 12 (0.327 m w.e. a⁻¹), respectively situated only 43 km northwest and 73 km southwest of Core
389 11. In the GPR data, the number of traceable IRHs is highest towards the interior of the ice sheet and lowest
390 in warmer areas towards the coast and in the south, where refrozen percolated melt water from enhanced
391 surface melt attenuates the radar signal and reduces the number of observable IRHs (Brown et al., 2011;
392 Figure 3).

393 **3.2. Validation with past measurements**

394 We validate our accumulation record with published core records from the PARCA campaign and
395 accumulation data from the NASA IceBridge program. The locations of GreenTrACS Core sites 2, 5, 9, 10,
396 11, 14, 15, and 16 were chosen to reoccupy PARCA core locations 6745, 6945, 7147, 7247, 7249, NASA-

397 U, 7347, and 7345, respectively. These GreenTrACS cores overlap with the accumulation history of each
 398 PARCA core and extend the record from 1997/1998 to 2016/2017. Accumulation rates derived from
 399 GreenTrACS firm cores are within error of those determined from corresponding PARCA cores during the
 400 period of overlap. Figure 5 compares the accumulation records from PARCA sites 6745, 6945, 7345, and
 401 NASA-U to their corresponding GreenTrACS cores, demonstrating that each pair of cores has similar long-
 402 term mean accumulation and nearly identical decadal variability. Thus, we have confidence in firm core
 403 derived accumulation rates that are used in subsequent GPR calculations of accumulation rates throughout
 404 the GreenTrACS traverse.

405



406

407 **Figure 5. Accumulation from GPR and collected firm cores (this study) compared with cores from the PARCA Campaign. Thin lines**
 408 **represent annual PARCA (blue) and GreenTrACS (black) firm core accumulation, while thick lines are 5-year averages over**
 409 **corresponding GPR epochs. Error bars represent one standard deviation over each epoch. GPR and PARCA accumulation averages**
 410 **and decadal trends are statistically indistinguishable.**

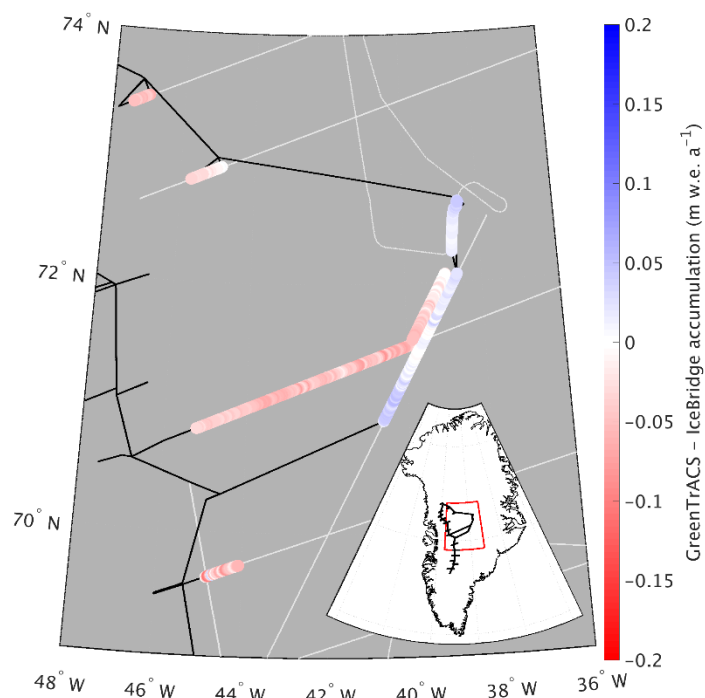
411

412 Average (1966 – 2016) GPR accumulation is statistically indistinguishable with average (1962 – 2014)
 413 IceBridge Accumulation Radar measurements analyzed by Lewis et al. (2017), with an RMS difference of
 414 0.0387 ± 0.0327 m w.e. a⁻¹ along a total of 562.5 km of overlap (Figure 6). The disagreement is largest at
 415 lower elevations, where Herron-Langway profiles used in Lewis et al. (2017) differ the most from
 416 GreenTrACS firm core density profiles in the upper 30 m of firm, demonstrating the importance of field
 417 observations for calibration and validation. The close agreement at higher elevations is illustrated in Figure
 418 7a, where our GreenTrACS accumulation measurements are statistically indistinguishable from the IceBridge

419 radar-derived accumulation (Lewis et al., 2017) along the 285 km A – A’ transect on Figure 1. Notice that
420 the uncertainty in GreenTrACS accumulation progressively decreases higher in the percolation zone and into
421 the dry snow zone (towards the right in Figure 7) along this transect as density becomes less heterogeneous
422 from fewer melt layers (Graeter et al., 2018) and IRHs become easier to trace.

423
424 Similarly, our 2011-2016 accumulation is statistically indistinguishable from average 2009 – 2012 IceBridge
425 snow radar measurements analyzed by Koenig et al. (2016), with an RMS difference of 0.0489 ± 0.0961 m
426 w.e. a⁻¹ along a total of 69.7 km of overlap (not shown). Koenig et al. (2016) use a different radar system on
427 an airborne platform and are able to calculate annual accumulation at elevations below 2000 m a.s.l., however
428 the GreenTrACS accumulation record covers a longer temporal duration than the data from that study.

429
430



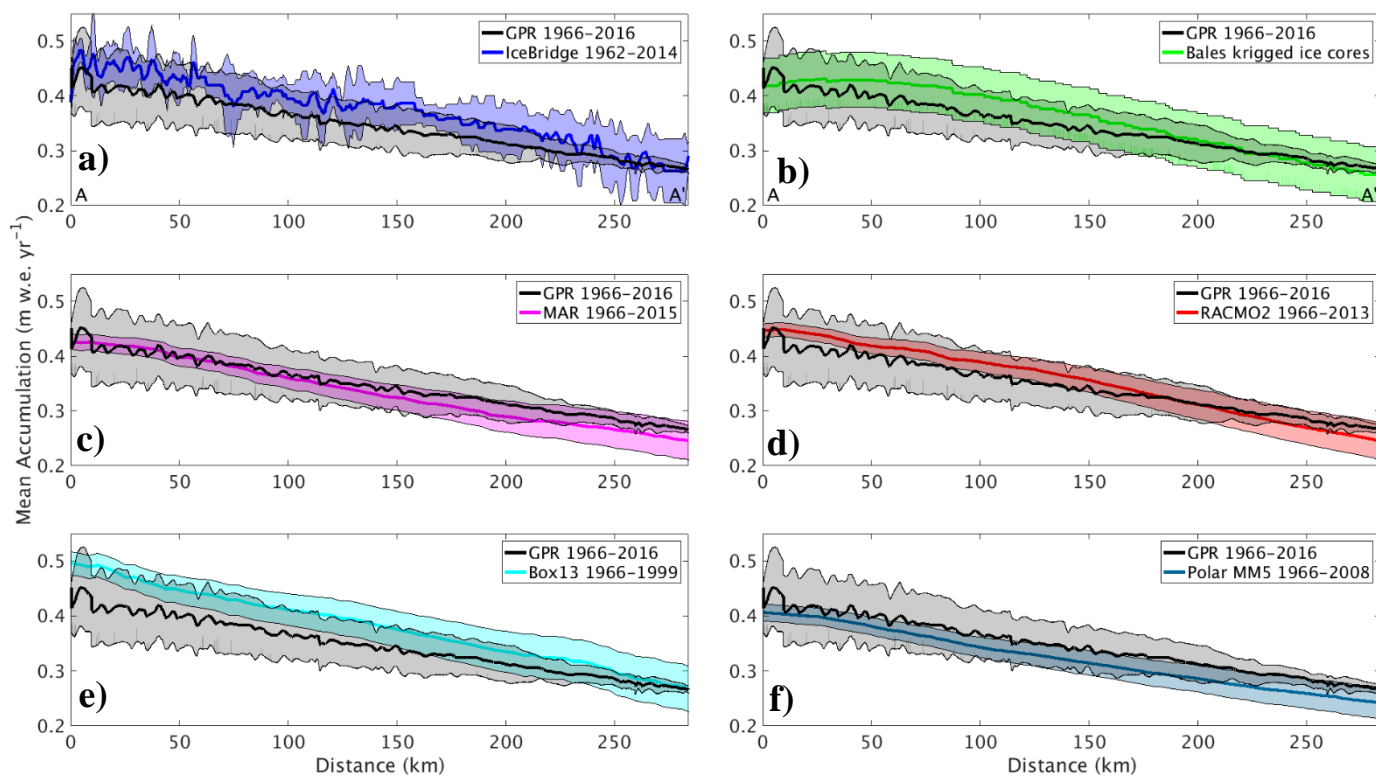
431
432 **Figure 6. Difference between averaged (1966 – 2016) GreenTrACS accumulation and average (1962 – 2014) IceBridge Accumulation**
433 **Radar rates from Lewis et al. (2017) across all 562.5 km of overlap. Spatially overlapping section of 2016 and 2017 traverses displayed**
434 **as adjacent tracks. Also showing extent of GreenTrACS traverse (black) and IceBridge accumulation radar (grey). Inset shows map**
435 **location with respect to GreenTrACS traverse (black).**

436

437 3.3. Comparison to modelled accumulation

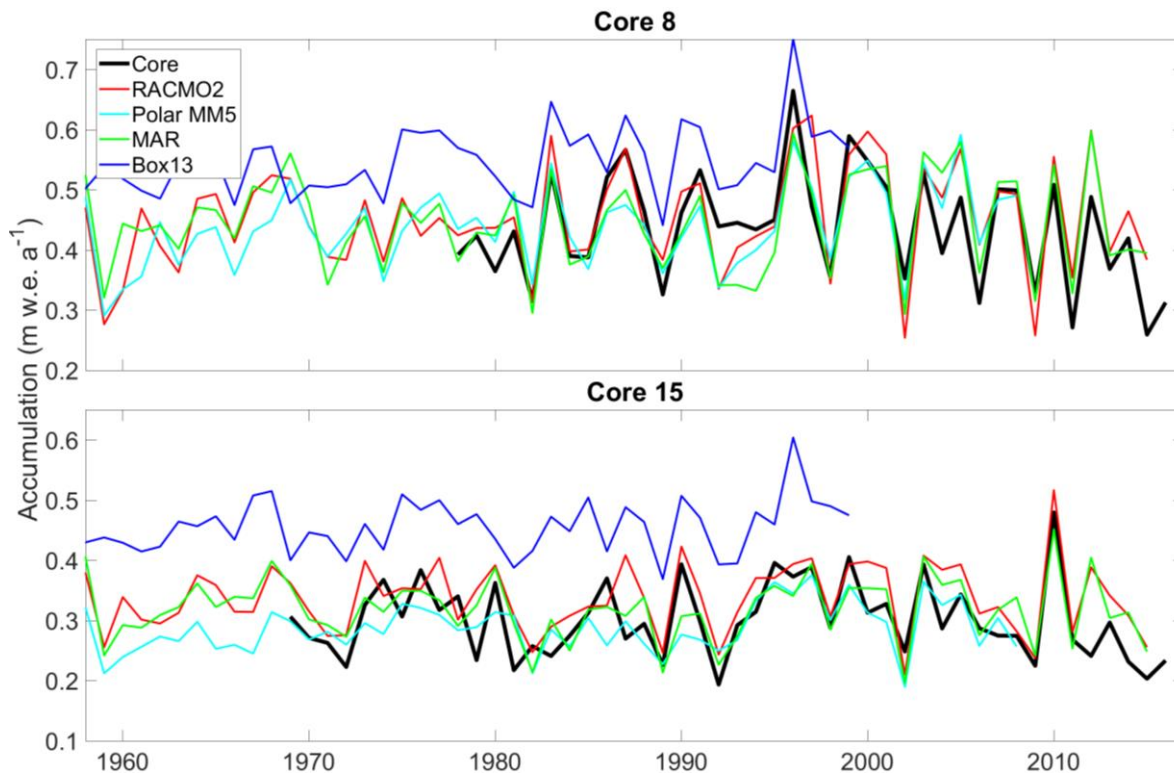
438 We assess differences between RCM accumulation output and GreenTrACS accumulation record at each firn
439 core site, two of which are shown in Figure 8. In general, year-to-year correlations between GreenTrACS
440 firn core accumulation records and RCM output for the corresponding grid cell are strong, positive, and

441 statistically significant (Table 2). On average, GreenTrACS firn cores' correlation coefficient with MAR
 442 output is 0.718, with PolarMM5 is 0.701, with Box13 is 0.607, and with RACMO2 is 0.763. Every correlation
 443 is statistically significant at $p < 0.05$ except for Cores 7 and 11 with Box13. We do not report a correlation
 444 coefficient for Core 11 and Box13 because they only share two common years. Temporal correlation
 445 coefficients remain high even at locations with large magnitude differences between RCM output and firn
 446 core accumulation. For example, the Box13 model overestimates accumulation at Core 15 by 0.15 ± 0.05 m
 447 w.e. a^{-1} , on average, but the model output has a correlation coefficient of 0.48 with Core 15 (Table 2) and
 448 matches years of high accumulation (e.g. 1987, 1990, and 1996) and low accumulation (e.g. 1981, 1989,
 449 1992).



450
 451 **Figure 7. Average GreenTrACS GPR accumulation (black) compared with a) IceBridge accumulation radar, b) Bales09 krigged ice core**
 452 **map, c) MAR, d) RACMO2, e) Box13, and f) Polar MM5. GPR measurements are statistically indistinguishable from each of the other**
 453 **measurements along this 285 km transect in the dry snow zone (A – A' on Figure 1).**

454



455

456 **Figure 8.** Accumulation record at GreenTrACS Core 8 and Core 15 (black) compared with RCM output from RACMO2 (red), Polar
 457 MM5 (cyan), MAR (green), and Box13 (blue). We find statistically significant Pearson correlation coefficients between GreenTrACS
 458 and RCM accumulation rates for these cores (see Table 2).

459

460 **Table 2.** Pearson correlation coefficients between accumulation rate time series from firn cores and co-located RCM output over their
 461 common time period[#].

	Available data period	MAR	PolarMM5	Box13	RACMO2
Core1	1966 – 2016	0.70	0.66	0.56	0.73
Core2	1969 – 2016	0.75	0.77	0.62	0.79
Core3	1971 – 2016	0.72	0.69	0.63	0.74
Core4	1977 – 2016	0.79	0.74	0.72	0.72
Core5	1984 – 2016	0.81	0.80	0.60	0.79
Core6	1985 – 2016	0.76	0.76	0.65	0.83
Core7	1993 – 2016	0.81	0.82	0.61	0.73
Core8	1978 – 2017	0.78	0.77	0.69	0.81
Core9	1984 – 2017	0.68	0.75	0.74	0.79
Core10	1984 – 2017	0.88	0.80	0.80	0.80
Core11	1997 – 2017	0.75	0.59	N/A	0.75
Core12	1962 – 2017	0.6	0.54	0.53	0.64
Core13	1955 – 2017	0.51	0.62	0.37	0.76
Core14	1974 – 2017	0.70	0.62	0.46	0.74
Core15	1969 – 2017	0.68	0.63	0.48	0.75
Core16	1979 – 2017	0.79	0.77	0.66	0.88

462 [#]Statistically significant correlations ($p < 0.05$) are bold

463

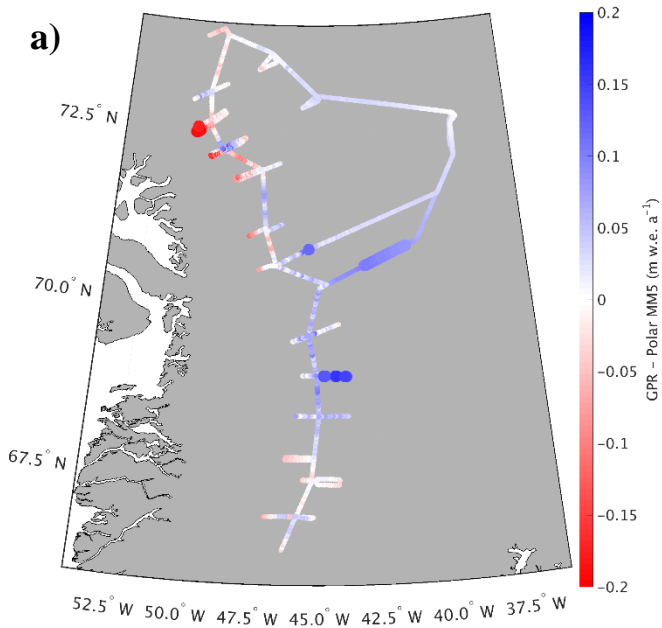
464 We also assess spatial differences between GreenTrACS accumulation and mean RCM accumulation
 465 averaged over several decades (Table 2). Figure 9 shows that differences between GreenTrACS accumulation

466 and RCM output increase in magnitude, become more spatially heterogeneous, and vary by model at lower
467 elevations of the ice sheet where topographic variations are larger and surface melt increases. Averaged over
468 all 4436 km of the traverse, the RMS difference ($\pm 1\sigma$) between each model and GreenTrACS accumulation
469 over corresponding data periods (Table 2) is 0.068 ± 0.065 (MAR), 0.0562 ± 0.0548 (RACMO2), $0.0822 \pm$
470 0.0702 (Box13), 0.048 ± 0.045 (Polar MM5), and 0.0475 ± 0.0445 m w.e. a^{-1} (Bales09). We find that RCM
471 differences from GreenTrACS accumulation are small in the dry snow zone (Figure 9). For example, Figure
472 7 shows that average GreenTrACS accumulation measurements from 1966 – 2016 along the A – A’ transect
473 in Figure 1 are statistically indistinguishable from those derived from the Bales09 krigged ice core map
474 (Figure 7b), MAR (1966 – 2015; Figure 7c), RACMO2 (1966 – 2013; Figure 7d), Box13 (1966 – 1999;
475 Figure 7e), and Polar MM5 (1966 – 2008; Figure 7f).

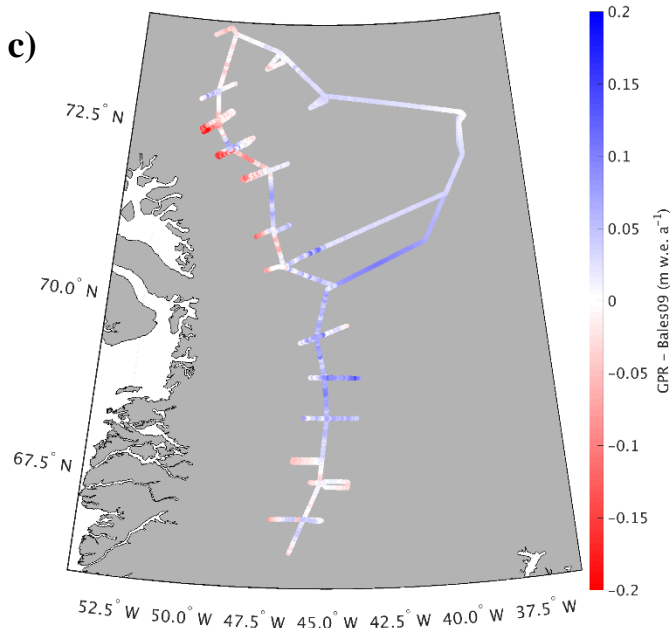
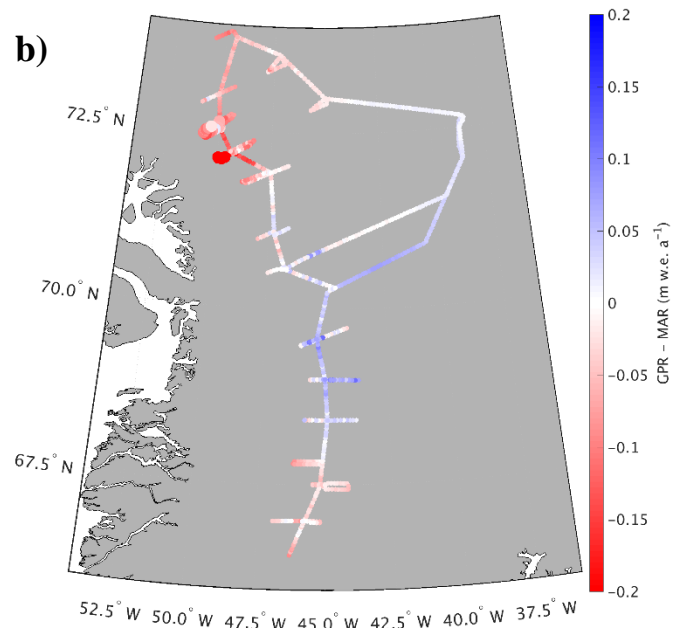
476
477 However, the high spatial resolution of our dataset shows significant accumulation variability not captured
478 in model output (Figure 9). For example, Polar MM5 and MAR both underestimate accumulation between
479 Core 4 and Summit, while overestimating accumulation to the west of Cores 10 – 12. Likewise, RACMO2
480 overestimates accumulation between Raven/Dye-2 and Core 5 by 0.03 to 0.08 m w.e. a^{-1} and shows
481 statistically significant differences east of Cores 11 and 12. Bales09 accurately calculates accumulation along
482 most of the 2016 traverse, but overestimates accumulation west of Cores 11 and 12 by 0.135 ± 0.041 m w.e.
483 a^{-1} . Finally, Box13 overestimates accumulation along many of the western spurs and has statistically
484 significant overestimations of 0.1 to 0.4 m w.e. a^{-1} between Cores 10 and 16. Box13 overestimates 67.8% of
485 the data in the Core 10 – 16 region by at least 0.1 m w.e. a^{-1} , and 6.6% of that data by at least 0.2 m w.e. a^{-1} .

486
487 Our study is almost entirely contained within drainage basin E from Vernon et al. (2013), who note that basin
488 E is the only major Greenland drainage basin with no statistically significant differences in SMB between
489 the four RCMs. However, differences of 0.1 to 0.4 m w.e. a^{-1} exist when we look at a local (sub-drainage-
490 basin) scale for each model. All four of the RCMs overestimate accumulation along the western spur of Core
491 11 and they all underestimate accumulation along the eastern spur of Core 5 (Figure 9).

492

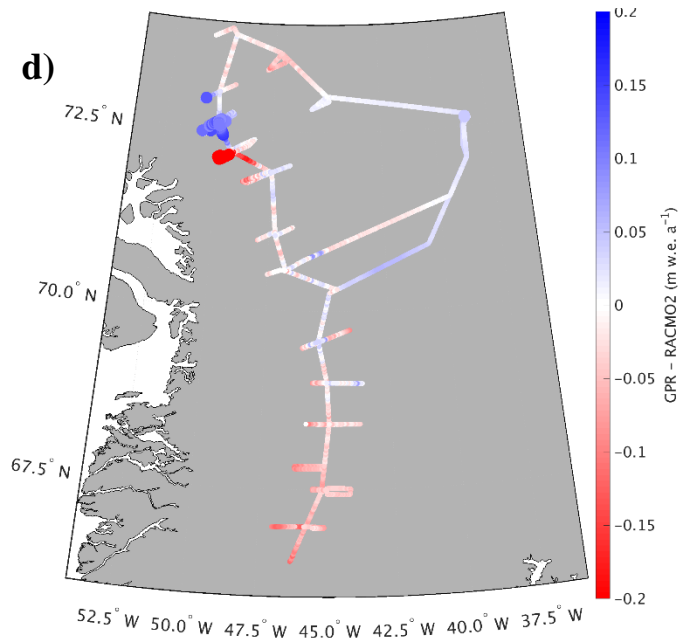


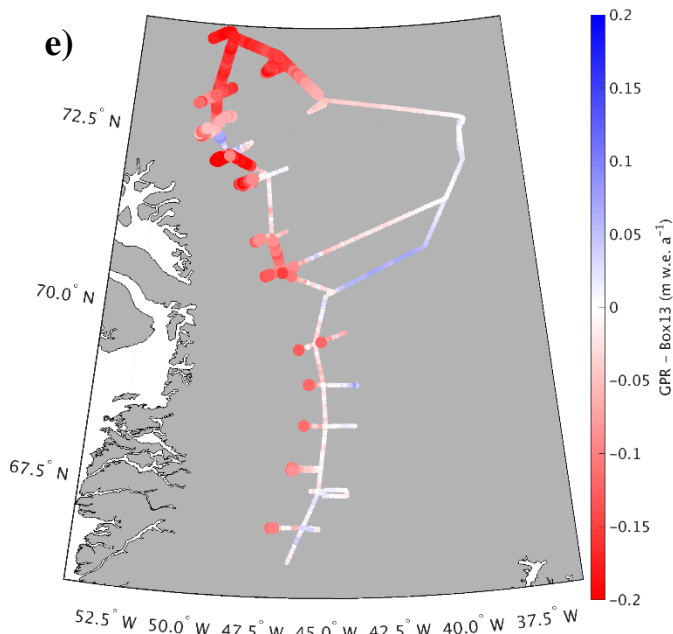
493



494

495





496
 497 **Figure 9. Differences between GreenTrACS accumulation and a) Polar MM5, b) MAR, c) Bales09, d) RACMO2, and e) Box13**
 498 **accumulation averaged over the corresponding time periods. Large dots show statistically significant differences from GreenTrACS**
 499 **accumulation.**

500
 501 In summary, the RCMs do an excellent job of calculating accumulation averaged over this drainage basin,
 502 with RMS values between 0.048 and 0.0822 m w.e. a⁻¹, but there are larger differences of 0.1 to 0.4 m w.e.
 503 a⁻¹ between model and GPR accumulation on local scales. Differences between GreenTrACS and RCM
 504 accumulation are largest in areas concurrent with the fewest, shortest, and/or most outdated *in situ*
 505 measurements. For example, the GPR vs. model differences near Cores 11, 12, and 13 are relatively large for
 506 all RCMs, despite Core 11 being co-located with PARCA 7249. However, the PARCA cores were collected
 507 over 20 years ago, and Core 11 only spanned 7 years because of the high accumulation rate at that site. This
 508 highlights the importance of collecting updated field-based measurements to calibrate remotely sensed data
 509 and RCM output.

511 3.4. Accumulation temporal trends

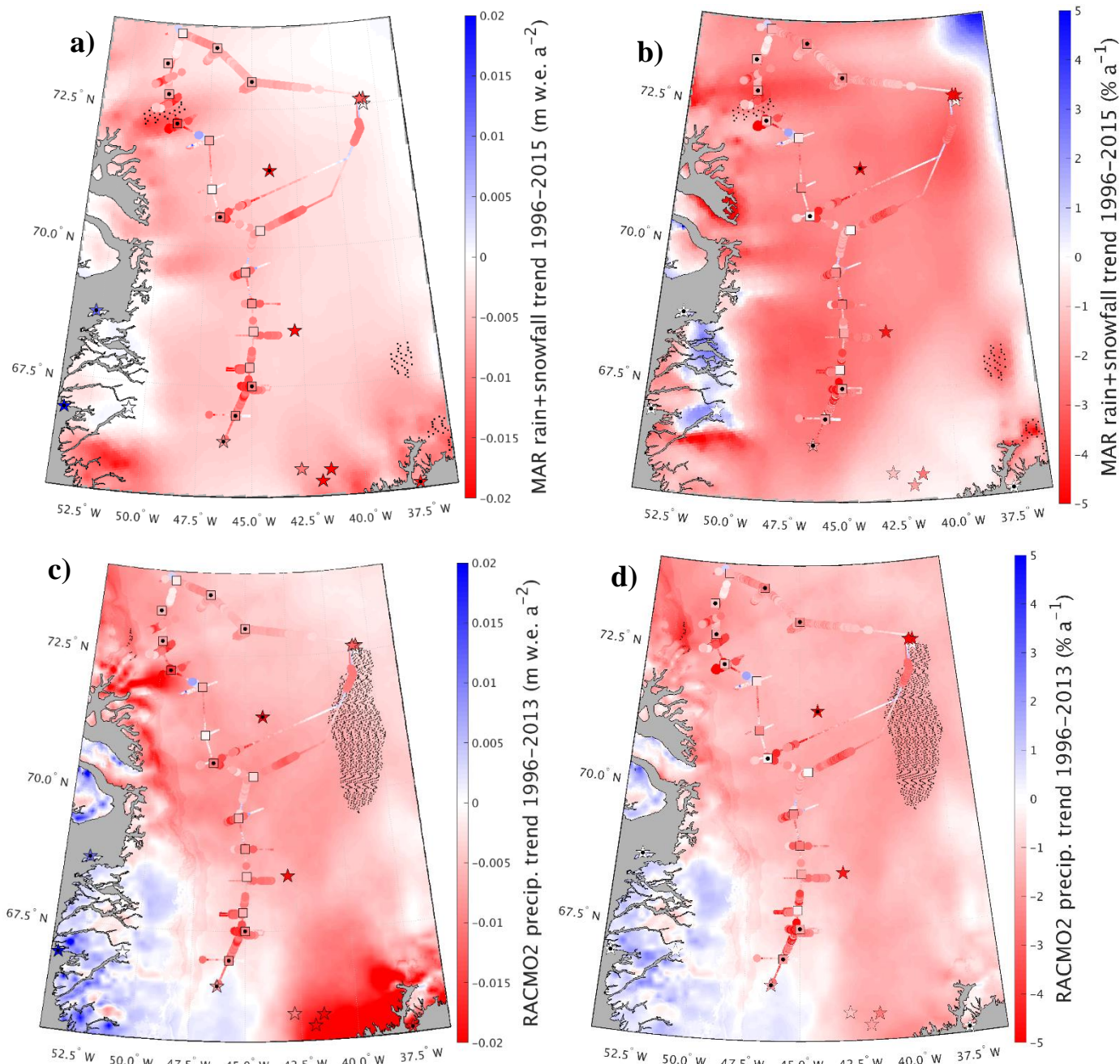
512 In most locations, there are no statistically significant trends in the GreenTrACS accumulation record from
 513 1966 through the mid-1990s. However, a changepoint analysis (Lavielle, 2005) reveals that accumulation in
 514 the Western GrIS percolation zone changed significantly after the 1995 – 1996 accumulation year. Since
 515 1996, our record indicates a statistically significant average accumulation decrease of 0.009 ± 0.005 m w.e
 516 a⁻², or 2.4 ± 1.5 % a⁻¹, from 1996 to 2017. Although we observe fewer statistically significant accumulation
 517 trends when we expand this analysis to include the entire temporal duration for each firn core, the sign of the
 518 trend at each core site does not change.

519

520 In Figure 10, we compare the negative accumulation trend in the GreenTrACS record (1996 – 2016) to best-
521 fit linear trends in total precipitation (rain + snowfall) across the ice sheet in MAR and RACMO2 simulations
522 over the 1996 – 2015 and 1996 – 2013 periods, respectively. Also shown in Figure 10 are 1996 – 2016
523 accumulation trends for all 16 GreenTrACS firn cores (squares), accumulation trends from ACT10A (1996
524 – 2010), ACT10B (1996 – 2010), ACT10C (1996 – 2010), D4 (1991 – 2002), D5 (1991 – 2002), Katie (1991
525 – 2002), Sandy (1991 – 2002), and Summit 2010 (1991 – 2010) ice/firn cores (stars on ice sheet), and
526 precipitation trends from coastal weather stations (Mernild et al., 2014; stars on coast). Statistically
527 significant trends ($p < 0.05$) in core data are indicated by black dots, while statistically significant trends in
528 the MAR and RACMO2 output are stippled in black.

529

530 We find strong agreement between the accumulation decrease in the GreenTrACS record and widespread
531 precipitation decreases in the RCMs over the study area (Figure 10). On average, the RCMs have a more
532 negative precipitation trend than the GreenTrACS record by 0.003 ± 0.005 for MAR and 0.0016 ± 0.0051 m
533 w.e. a^{-2} for RACMO2. Vernon et al. (2013) show a melt-driven decrease in SMB across this drainage basin
534 of 31.1% (ECMWFd), 61.6% (RACMO2), 76.5% (MAR), and 33.5% (Polar MM5) for the 1996 – 2008
535 period. The negative precipitation trends of $2.4 \pm 1.5 \%$ a^{-1} (Figure 10d) indicate a total of 2539.4 fewer Gt
536 of precipitation and a total of 5159.1 additional Gt of melt (not shown) over 1996 – 2013 across the GrIS.
537 Thus, our analysis suggests that a significant decline in snow accumulation contributes to declining SMB
538 throughout the Western GrIS over recent decades, in addition to increasing surface melt from rising
539 temperatures (van den Broeke et al., 2009, 2016).



540

541

542

543

544

545

546

547

548

3.5. Effects of melt on accumulation trends

549

550

551

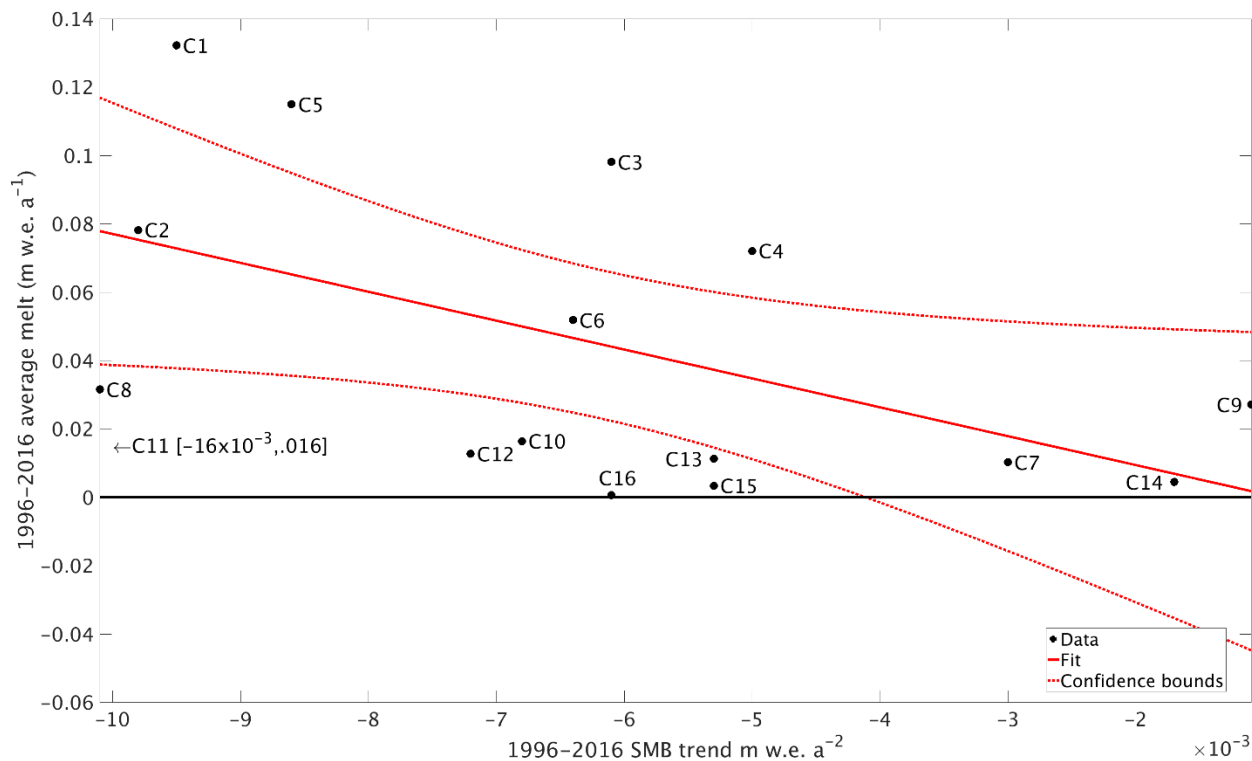
Increased melt throughout the 1996 – 2016 period is a confounding variable when analyzing trends in accumulation. With increased melt over the past several decades in this region, meltwater percolates down through several years of firm (Benson, 1962; Graeter et al., 2018; Harper et al., 2012; Wong et al., 2013).

552 This movement of mass into lower years can artificially increase the mass balance at depth and lower the
553 mass balance during the most recent years, which have not experienced as much meltwater percolation from
554 more recent annual layers. Therefore, it is necessary to evaluate the degree to which the recent accumulation
555 decrease in the GreenTrACS record is biased by the recent increase in surface melt and percolation.

556
557 Figure 11 compares the 1996 – 2016 mass balance trends with 1996 – 2016 average melt for each of the
558 sixteen GreenTrACS firn cores. If we exclude Core 11 (which only dates back to 1997 and has a highly
559 negative SMB trend), the linear regression is statistically significant with $p = 0.04$ (Figure 11). Note that both
560 the measured Core 11 SMB trend and RCM trends at that location are so negative, with that small amount of
561 average melt, that the linear trend is no longer significant if that point is included in the calculations. On
562 average, we find larger negative accumulation trends (-7×10^{-3} to -10×10^{-3} m w.e. a^{-2}) at the lower latitude
563 cores that experience more melt, supporting the hypothesis that meltwater percolation and refreezing are
564 enhancing the negative accumulation trend.

565
566 However, several other lines of evidence support a negative accumulation trend in the study area since 1996.
567 First, we find statistically significant negative accumulation trends at Cores 10, 11, 12, 13, 15, and 16, each
568 of which experience $< 1.6 \text{ cm } a^{-1}$ of meltwater percolation on average (Figure 11). Additionally, we have
569 confidence that GreenTrACS accumulation trends reported here are not artifacts of meltwater percolation
570 because both MAR and RACMO2 have similar trends in precipitation (Figure 10). Finally, we evaluate the
571 maximum effect meltwater percolation could have on GreenTrACS accumulation trends over 1996 – 2016.
572 The largest measured melt layer from our sixteen ice cores occurred during 2003 – 2004 in Core 1 and
573 contains 0.364 m of ice, equivalent to 0.333 m w.e. (Graeter et al., 2018). We add this percolation to nine
574 years' of accumulation using a sine wave (percolation magnitude 0, 0.5, 1, 0.5, 0, -0.5, -1, -0.5, 0), square
575 wave (0, 0, 0, 1, 1, 1, 0, 0, 0), and triangle wave (0, 0.25, 0.5, 0.75, 1, 0.75, 0.5, 0.25, 0) weighted kernel,
576 before re-computing hypothetical accumulation trends over the same time period with additional meltwater
577 percolation. Regardless of the wave-type choice, re-calculated trends remain within a factor of two of the
578 original SMB trends and do not change sign with additional percolation.

579



580

581 **Figure 11. Relationship between 1996 – 2016 SMB trend and 1996 – 2016 melt for each of the 16 GreenTrACS firn cores (black circles).**
 582 **Red line shows linear best fit, dotted line shows 95% confidence boundary.**

583

3.6. Atmospheric circulation drivers of the recent accumulation decline

584

585 Our analysis indicates that snow accumulation has been declining in Western Greenland since 1996, despite
 586 significant warming and resulting increases in saturation vapor pressure from the Clausius-Clapeyron
 587 relationship. Instead, precipitation decreases over Western Greenland likely result from changes in
 588 atmospheric and/or oceanic circulation. Mernild et al. (2014) and Auger et al. (2017) found that the positive
 589 phase of the Atlantic Multidecadal Oscillation (AMO) is associated with a precipitation increase over interior
 590 and Southwestern Greenland based on ice core records and the Japanese Meteorological Agency 55 Year
 591 Reanalysis (JRA-55; Kobayashi et al., 2015), respectively. In direct contrast with these findings, the decline
 592 in Western Greenland accumulation documented in the GreenTrACS record began in the mid-1990s,
 593 contemporaneous with a switch to the AMO positive phase.

594

595 We hypothesize that the differences between our results and those of Auger et al. (2017) and Mernild et al.
 596 (2014) stem from different causes. Auger et al. (2017) validated the reanalysis data by demonstrating that
 597 JRA-55 precipitation at Nuuk, Greenland is significantly correlated with Nuuk station data from 1958 – 2013.
 598 Furthermore, coastal precipitation in Western Greenland is strongly and significantly ($p < 0.05$) correlated
 599 with precipitation over the interior Western GrIS in the JRA-55 dataset (not shown). However, Mernild et al.
 (2014) found that coastal Greenland precipitation is anti-correlated with ice core accumulation records from

600 the interior GrIS from 1900 to 2000. This suggests that JRA-55 precipitation data, which is not constrained
601 by ice core accumulation records, should be interpreted with caution over the interior GrIS. Mernild et al.
602 (2014) concluded that positive AMO conditions favor higher precipitation over the interior GrIS based on
603 the previous positive AMO phase (1920s to mid-1960s), contrasting with lower accumulation during the
604 negative AMO phases (mid-1960s to mid-1990s and prior to the 1920s). However, Mernild et al. (2014) state
605 that the ice core composite record in their analysis may be biased from 1995 – 2000, and they do not analyze
606 precipitation trends after 2000. Thus, the decline in Western GrIS accumulation documented in the
607 GreenTrACS cores during the latest positive AMO phase from 1996 to 2017 was not captured in the Mernild
608 et al. (2014) analysis. Our results suggest that factors other than the AMO are behind the decline in Western
609 GrIS accumulation since 1996.

610
611 We find that the decrease in accumulation over the Western GrIS is associated with a significant decrease in
612 the number of storm-days since 1996. The GreenTrACS region experienced an average of 115.8 ± 15.3 storm-
613 days per year over 1958 – 1996 and 96.2 ± 27.3 storm-days per year over 1996 – 2016. A two sample t-test
614 indicates that this 17% decline in storm-days is statistically significant ($p < 0.001$). The largest decrease in
615 storm-days (25%) over the GreenTrACS region occurred during summer, with 56.4 ± 6.1 storm-days per
616 summer from 1958 – 1996 and 42.3 ± 17.4 storm-days per summer from 1996 – 2016 ($p < 0.0001$; Figure
617 12b). We also find an increase in the number of storm-days in the Northwestern GrIS near Thule (not shown).

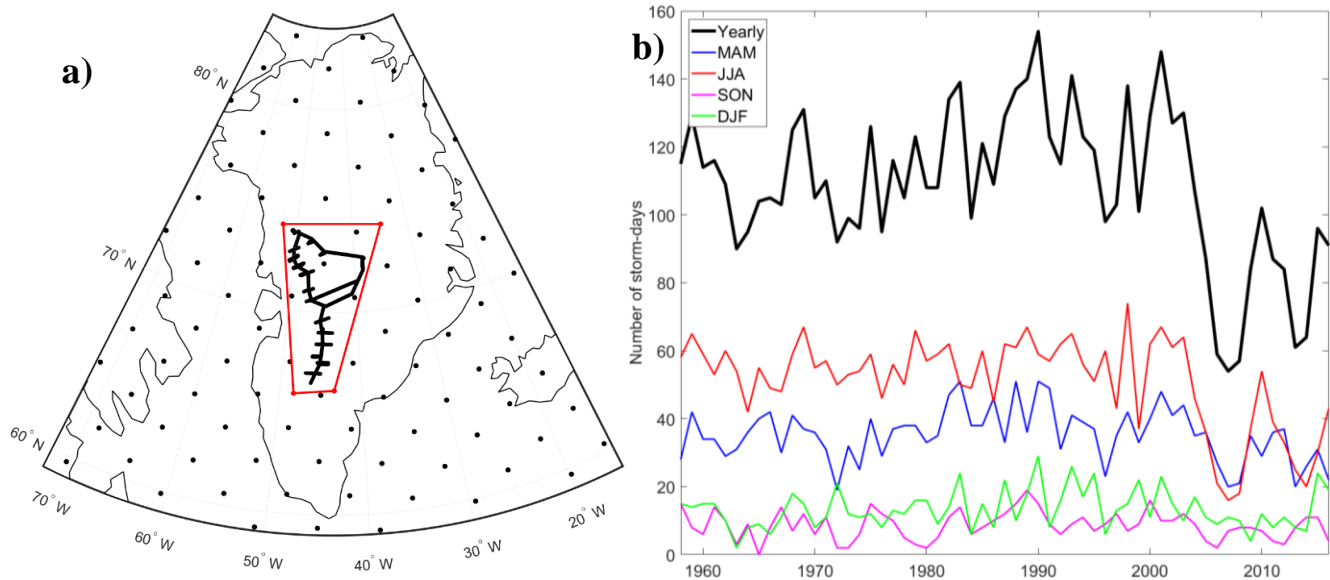
618
619 The decline in summer storm-days indicates a relationship with well-documented stronger summer blocking
620 over Greenland over the past two decades (Hanna et al., 2013; McLeod and Mote, 2016), with a positive
621 Greenland Blocking Index (GBI) during 17 out of 21 summers between 1996 – 2016 (Hanna et al., 2016).
622 The June – August GBI had a statistically significant positive trend of 1.87 (unitless; normalized to 1951 –
623 2000) from 1991 – 2015 (Hanna et al., 2016). The summertime 500 mbar geopotential height increased 50 –
624 70 m over the 1996 – 2016 period compared with the 1979 – 1996 baseline (Figure 12c), indicating stronger
625 blocking that we suggest likely reduced precipitation over the central GrIS by deflecting storms poleward
626 from the Greenland interior. This is consistent with an observed $0.9 \pm 0.3\% \text{ a}^{-1}$ decrease in JJA cloud cover
627 over Greenland from 1995-2009, with the largest decreases in the GreenTrACS region (Hofer et al., 2017).
628 Furthermore, we find a strong negative correlation between ERA-Interim 1979 – 2015 June – August (JJA)
629 GBI and JJA precipitation in both MAR (Figure 12d) and RACMO2 (not shown) across the central and
630 southern GrIS. These results suggest that the blocking-induced accumulation decline observed in the
631 GreenTrACS region is representative of a broader pattern over the GrIS, with the exception of Northwest
632 Greenland where poleward blocking has increased storm-days (not shown) and accumulation (Figure 12d).

633

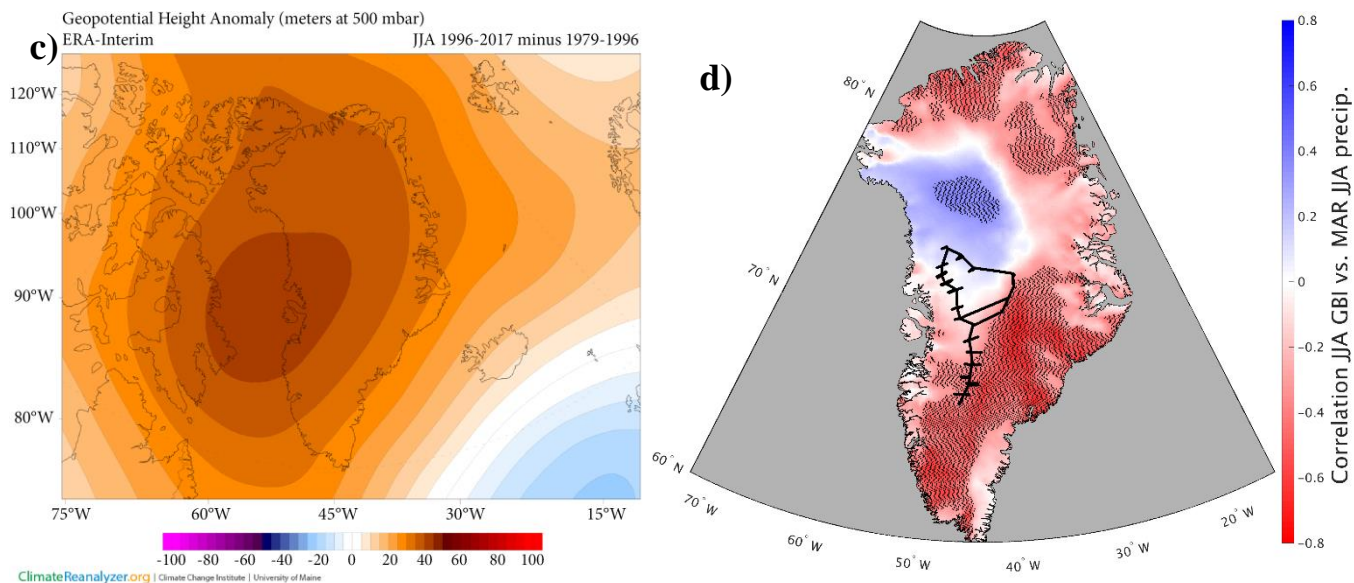
634

635 The effect of summertime Greenland blocking has previously been discussed primarily in the context of
636 increasing surface melt (Hanna et al., 2013; Ballinger et al., 2017; Hanna et al., 2018; Hofer et al., 2017),
637 while the effect of blocking on precipitation has received less attention (Hanna et al., 2013; McLeod and
638 Mote, 2016). Our results highlight that stronger summer blocking reduces GrIS SMB through both an
639 increase in surface melting and a decrease in accumulation. Stronger summer blocking has been tied to an
640 observed increase in surface melt since 1996 across the Western GrIS percolation zone (Graeter et al., 2018),
641 and to the July 2012 melt event, during which 98.6% of the GrIS experienced melt (Nghiem et al., 2012). We
642 show here with *in situ* data that snow accumulation has declined in this same region as strong blocking has
643 decreased the number of summer storm-days. Presently, none of the GBI outputs from the Coupled Model
644 Intercomparison Project 5 (CMIP5) suite of global climate models accurately capture the recent summer GBI
645 increase (Hanna et al., 2018). Improved predictions of summertime Greenland blocking under future
646 anthropogenic forcing scenarios are therefore critical for accurately predicting Greenland SMB and its
647 contribution to sea level rise.

648



649



650

651

652 **Figure 12. a) (Serreze, 2009) gridded storm track dataset showing location of GreenTrACS traverse and inquiry box. b) Total number of storm-days within inquiry box for annual and seasonal periods. Horizontal black lines show a decrease in 1958 – 1996 to 1996 – 2016**
 653 **average number of storm-days within this region. c) 500 mbar geopotential height change over Greenland showing 1996 – 2016 minus**
 654 **1979 – 1996 for the summer season. Image obtained using Climate Reanalyzer (<http://cci-reanalyzer.org>), Climate Change Institute,**
 655 **University of Maine, United States. d) Correlation between June – August Greenland Blocking Index and MAR June – August**
 656 **precipitation. Statistically significant RCM grid cell correlations are stippled black. GreenTrACS traverse is shown in black.**
 657

658 4. Conclusions

659 We have developed a new dataset of accumulation rates over the western interior of the Greenland ice sheet
 660 spanning the past 20 – 60 years, based on sixteen 22 – 32 m long firn cores and 4436 km of *in situ* GPR
 661 accumulation data. This accumulation record is internally consistent across the dataset and is validated by
 662 previous *in situ* field measurements and other radar-derived accumulation measurements (e.g Lewis et al.,
 663 2017).

664

665 Overall, the Polar MM5 (Burgess et al., 2010), MAR (Fettweis et al., 2016), Box13 (Box et al., 2013), and
 666 RACMO2 (Noël et al., 2018) Regional Climate Models accurately capture large spatial patterns in
 667 accumulation over the GrIS, but show statistically significant differences from GPR accumulation on a
 668 regional basis. The average RMS difference between each model and GreenTrACS accumulation is $0.068 \pm$
 669 0.065 (MAR), 0.048 ± 0.045 (Polar MM5), 0.0822 ± 0.0702 (Box13), 0.0562 ± 0.0548 (RACMO2), and
 670 0.0475 ± 0.0445 m w.e. a^{-1} (Bales09). These differences are on the same order as the uncertainties in the
 671 GreenTrACS and RCM accumulation estimates. While these average differences are small, we find
 672 differences of 0.1 to 0.4 m w.e. a^{-1} when we investigate at a local scale for each model.

673

674 While global climate models predict a 21st-century increase in precipitation over the GrIS (e.g. Bintanja and
675 Selten, 2014), we observe a decrease in precipitation across the Western GrIS from 1996 – 2016 using records
676 from firn cores, GPR, and published RCMs. We believe this study is the first to identify widespread negative
677 GrIS precipitation trends during this period of enhanced surface melt, evident in these RCMs and our field
678 observations (Graeter et al., 2018).

679

680 We attribute the decrease in accumulation over the Western GrIS between 1996 and 2016 to more persistently
681 positive Greenland blocking in the summer. We find a statistically significant 25% reduction in the number
682 of summer storms that precipitate over the GreenTrACS region since 1996. While warming temperatures
683 from anthropogenic forcing and enhanced summer blocking have increased melt across the western
684 percolation zone, here we show that summer blocking has also contributed to declining precipitation over the
685 past two decades. This has led to a strongly negative SMB trend on both the input and output sides of the
686 SMB equation that may not be accurately captured in global climate models that are currently unable to
687 reproduce the recent increase in blocking. This highlights the importance of improving GCM projections of
688 future summer blocking to accurately forecast Greenland precipitation and melt rates under stronger
689 greenhouse gas forcing.

690 **5. Works cited**

691 Auger, J. D., Birkel, S. D., Maasch, K. A., Mayewski, P. A. and Schuenemann, K. C.: Examination of
692 precipitation variability in southern Greenland, *J. Geophys. Res.*, 122(12), 6202–6216,
693 doi:10.1002/2016JD026377, 2017.

694 Bales, R. C., Guo, Q., Shen, D., McConnell, J. R., Du, G., Burkhart, J. F., Spikes, V. B., Hanna, E. and
695 Cappelen, J.: Annual accumulation for Greenland updated using ice core data developed during 2000-2006
696 and analysis of daily coastal meteorological data, *J. Geophys. Res. Atmos.*, 114(6), D06116,
697 doi:10.1029/2008JD011208, 2009.

698 Ballinger, T. J., Hanna, E., Hall, R. J., Cropper, T. E., Miller, J., Ribergaard, M. H., Overland, J. E. and
699 Høyer, J. L.: Anomalous blocking over Greenland preceded the 2013 extreme early melt of local sea ice,
700 *Ann. Glaciol.*, 2013(March 2013), 1–10, doi:10.1017/aog.2017.30, 2017.

701 Benson, C. S.: Stratigraphic studies in the snow and firn of the Greenland Ice Sheet, *Folia Geogr. Danica*, 9,
702 13–37, 1962.

703 Bevington, P. R. and Robinson, D. K.: *Data Reduction and Error Analysis for the Physical Sciences*, 2nd
704 Editio., McGraw-Hill., 1992.

705 Bintanja, R. and Selten, F. M.: Future increases in Arctic precipitation linked to local evaporation and sea-
706 ice retreat, *Nature*, 509(7501), 479–482, doi:10.1038/nature13259, 2014.

707 Box, J. E., Bromwich, D. H., Veenhuis, B. a., Bai, L. S., Stroeve, J. C., Rogers, J. C., Steffen, K., Haran, T.
708 and Wang, S. H.: Greenland Ice Sheet Surface Mass Balance Variability (1988 – 2004) from Calibrated
709 Polar MM5 Output *, *J. Clim.*, 19(12), 2783–2801, doi:doi.org/10.1175/JCLI3738.1, 2006.

710 Box, J. E., Cressie, N., Bromwich, D. H., Jung, J. H., van den Broeke, M. R., van Angelen, J. H., Forster, R.
711 R., Miège, C., Mosley-Thompson, E., Vinther, B. and McConnell, J. R.: Greenland ice sheet mass balance
712 reconstruction. Part I: Net snow accumulation (1600–2009), *J. Clim.*, 26(11), 3919–3934, doi:10.1175/JCLI-
713 D-12-00373.1, 2013.

714 van den Broeke, M. R., Bamber, J. L., Ettema, J., Rignot, E. J., Schrama, E., van de Berg, W. J., van
715 Meijgaard, E., Velicogna, I. and Wouters, B.: Partitioning recent Greenland mass loss., *Science*, 326(5955),
716 984–6, doi:10.1126/science.1178176, 2009.

717 van den Broeke, M. R., Enderlin, E. M., Howat, I. M., Kuipers Munneke, P., Noël, B., van de Berg, W. J.,
718 van Meijgaard, E. and Wouters, B.: On the recent contribution of the Greenland ice sheet to sea level change,
719 *Cryosph. Discuss.*, 1–26, doi:10.5194/tc-2016-123, 2016.

720 Brown, J., Harper, J., Pfeffer, W. T., Humphrey, N. and Bradford, J.: High-resolution study of layering within
721 the percolation and soaked facies of the Greenland ice sheet, *Ann. Glaciol.*, 52(59), 35–42,
722 doi:10.3189/172756411799096286, 2011.

723 Brown, J., Bradford, J., Harper, J., Pfeffer, W. T., Humphrey, N. and Mosley-Thompson, E.: Georadar-
724 derived estimates of firn density in the percolation zone, western Greenland ice sheet, *J. Geophys. Res. Earth*
725 *Surf.*, 117(1), 1–14, doi:10.1029/2011JF002089, 2012.

726 Buchardt, S. L., Clausen, H. B., Vinther, B. M. and Dahl-Jensen, D.: Investigating the past and recent $\delta^{18}O$ -
727 accumulation relationship seen in Greenland ice cores, *Clim. Past*, 8(6), 2053–2059, doi:10.5194/cp-8-2053-
728 2012, 2012.

729 Burgess, E. W., Forster, R. R., Box, J. E., Mosley-Thompson, E., Bromwich, D. H., Bales, R. C. and Smith,
730 L. C.: A spatially calibrated model of annual accumulation rate on the Greenland Ice Sheet (1958–2007), *J.*
731 *Geophys. Res. Earth Surf.*, 115(2), 1–14, doi:10.1029/2009JF001293, 2010.

732 Enderlin, E. M., Howat, I. M., Jeong, S., Noh, M. J., Van Angelen, J. H. and Van Den Broeke, M. R.: An
733 improved mass budget for the Greenland ice sheet, *Geophys. Res. Lett.*, 41(3), 866–872,
734 doi:10.1002/2013GL059010, 2014.

735 Fettweis, X., Box, J. E., Agosta, C., Amory, C., Kittel, C. and Gallée, H.: Reconstructions of the 1900–2015
736 Greenland ice sheet surface mass balance using the regional climate MAR model, *Cryosph. Discuss.*,
737 (November), 1–32, doi:10.5194/tc-2016-268, 2016.

738 Gerlitz, K., Knoll, M., Cross, G., Luzitano, R. and Knight, R.: Processing Ground Penetrating Radar Data to
739 Improve Resolution of Near-Surface Targets, in *Symposium on the Application of Geophysics to*
740 *Engineering and Environmental Problems 1993*, pp. 561–574, Environment and Engineering Geophysical
741 Society., 1993.

742 Graeter, K. A., Osterberg, E. C., Ferris, D., Hawley, R. L., Marshall, H. P. and Lewis, G.: Ice Core Records
743 of West Greenland Surface Melt and Climate Forcing, *Geophys. Res. Lett.*, doi:10.1002/2017GL076641,
744 2018.

745 Hall, D. K., Comiso, J. C., DiGirolamo, N. E., Shuman, C. A., Key, J. R. and Koenig, L. S.: A satellite-
746 derived climate-quality data record of the clear-sky surface temperature of the Greenland ice sheet, *J. Clim.*,
747 25(14), 4785–4798, 2012.

748 Hall, D. K., Comiso, J. C., DiGirolamo, N. E., Shuman, C. A., Box, J. E. and Koenig, L. S.: Variability in
749 the surface temperature and melt extent of the Greenland ice sheet from MODIS, *Geophys. Res. Lett.*, 40(10),
750 2114–2120, doi:10.1002/grl.50240, 2013.

751 Hanna, E., Mernild, S. H., Cappelen, J. and Steffen, K.: Recent warming in Greenland in a long-term
752 instrumental (1881–2012) climatic context: I. Evaluation of surface air temperature records, *Environ. Res.*
753 *Lett.*, 7(4), 045404, doi:10.1088/1748-9326/7/4/045404, 2012.

- 754 Hanna, E., Jones, J. M., Cappelen, J., Mernild, S. H., Wood, L., Steffen, K. and Huybrechts, P.: The influence
755 of North Atlantic atmospheric and oceanic forcing effects on 1900-2010 Greenland summer climate and ice
756 melt/runoff, *Int. J. Climatol.*, 33(4), 862–880, doi:10.1002/joc.3475, 2013.
- 757 Hanna, E., Cropper, T. E., Hall, R. J. and Cappelen, J.: Greenland Blocking Index 1851-2015: a regional
758 climate change signal, *Int. J. Climatol.*, 36(15), 4847–4861, doi:10.1002/joc.4673, 2016.
- 759 Hanna, E., Fettweis, X. and Hall, R. J.: Recent changes in summer Greenland blocking captured by none of
760 the CMIP5 models, *Cryosph. Discuss.*, 1–8, doi:10.5194/tc-2018-91, 2018.
- 761 Harper, J., Humphrey, N., Pfeffer, W. T., Brown, J. and Fettweis, X.: Greenland ice-sheet contribution to
762 sea-level rise buffered by meltwater storage in firn, *Nature*, 491(7423), 240–243, doi:10.1038/nature11566,
763 2012.
- 764 Hawley, R. L., Courville, Z. R., Kehrl, L. M., Lutz, E. R., Osterberg, E. C., Overly, T. B. and Wong, G. J.:
765 Recent accumulation variability in northwest Greenland from ground-penetrating radar and shallow cores
766 along the Greenland Inland Traverse, *J. Glaciol.*, 60(220), 375–382, doi:10.3189/2014JoG13J141, 2014.
- 767 Herron, M. M. and Langway, C. C.: Firn densification: an empirical model., *J. Glaciol.*, 25(93), 373–385,
768 doi:10.3198/1980JoG25-93-373-385, 1980.
- 769 Hofer, S., Bamber, J., Tedstone, A. and Fettweis, X.: Decreasing clouds drive mass loss on the Greenland
770 Ice Sheet, *EGU Gen. Assem. Conf. Abstr.*, 19(6), 5086, 2017.
- 771 Karlöf, L., Isaksson, E., Winther, J. G., Gundestrup, N. S., Meijer, H. A. J., Mulvaney, R., Pourchet, M.,
772 Hofstede, C., Lappégard, G., Petterson, R., van den Broeke, M. R. and Van De Wal, R. S. W.: Accumulation
773 variability over a small area in east Dronning Maud Land, Antarctic, as determined from shallow firn cores
774 and snow pits: Some implications for ice-core records, *J. Glaciol.*, 51(174), 343–352,
775 doi:10.3189/172756505781829232, 2005.
- 776 Kobayashi, S., Ota, Y., Harada, Y., Ebita, A., Moriya, M., Onoda, H., Onogi, K., Kamahori, H., Kobayashi,
777 C., Endo, H., Miyaoka, K. and Takahashi, K.: The JRA-55 Reanalysis: General Specifications and Basic
778 Characteristics, *J. Meteorol. Soc. Japan. Ser. II*, 93(1), 5–48, doi:10.2151/jmsj.2015-001, 2015.
- 779 Koenig, L. S., Ivanoff, A., Alexander, P. M., MacGregor, J. A., Fettweis, X., Panzer, B., Paden, J. D., Forster,
780 R. R., Das, I., McConnell, J. R., Tedesco, M., Leuschen, C. and Gogineni, S. P.: Annual Greenland
781 accumulation rates (2009–2012) from airborne snow radar, *Cryosph.*, 10(4), 1739–1752, doi:10.5194/tc-10-
782 1739-2016, 2016.
- 783 Kovacs, A., Gow, A. J. and Morey, R. M.: The in-situ dielectric constant of polar firn revisited, *Cold Reg.
784 Sci. Technol.*, 23(3), 245–256, doi:10.1016/0165-232X(94)00016-Q, 1995.
- 785 De La Peña, S., Howat, I. M., Nienow, P. W., Van Den Broeke, M. R., Mosley-Thompson, E., Price, S. F.,
786 Mair, D., Noël, B. and Sole, A. J.: Changes in the firn structure of the western Greenland Ice Sheet caused
787 by recent warming, *Cryosphere*, 9(3), 1203–1211, doi:10.5194/tc-9-1203-2015, 2015.
- 788 Lavielle, M.: Using penalized contrasts for the change-point problem, *Signal Processing*, 85(8), 1501–1510,
789 doi:10.1016/j.sigpro.2005.01.012, 2005.
- 790 Lewis, G., Osterberg, E. C., Hawley, R. L., Whitmore, B., Marshall, H. P. and Box, J. E.: Regional Greenland
791 accumulation variability from Operation IceBridge airborne accumulation radar, *Cryosph.*, 11(2), 773–788,
792 doi:10.5194/tc-11-773-2017, 2017.
- 793 McLeod, J. T. and Mote, T. L.: Linking interannual variability in extreme Greenland blocking episodes to
794 the recent increase in summer melting across the Greenland ice sheet, *Int. J. Climatol.*, 36(3), 1484–1499,
795 doi:10.1002/joc.4440, 2016.
- 796 Medley, B., Joughin, I., Das, S. B., Steig, E. J., Conway, H., Gogineni, S. P., Criscitiello, a. S., McConnell,

797 J. R., Smith, B. E., van den Broeke, M. R., Lenaerts, J. T. M., Bromwich, D. H. and Nicolas, J. P.: Airborne-
798 radar and ice-core observations of annual snow accumulation over Thwaites Glacier, West Antarctica
799 confirm the spatiotemporal variability of global and regional atmospheric models, *Geophys. Res. Lett.*,
800 40(14), 3649–3654, doi:10.1002/grl.50706, 2013.

801 Mernild, S. H., Hanna, E., McConnell, J. R., Sigl, M., Beckerman, A. P., Yde, J. C., Cappelen, J., Malmros,
802 J. K. and Steffen, K.: Greenland precipitation trends in a long-term instrumental climate context (1890-2012):
803 Evaluation of coastal and ice core records, *Int. J. Climatol.*, doi:10.1002/joc.3986, 2014.

804 Meyer, C. R. and Hewitt, I. J.: A continuum model for meltwater flow through compacting snow, *Cryosphere*,
805 11(6), 2799–2813, doi:10.5194/tc-11-2799-2017, 2017.

806 Morlighem, M., Rignot, E. J., Mouginit, J., Seroussi, H. and Larour, E.: Deeply incised submarine glacial
807 valleys beneath the Greenland ice sheet, *Nat. Geosci.*, 7(6), 18–22, doi:10.1038/ngeo2167, 2014.

808 Morris, E. M. and Wingham, D. J.: Densification of polar snow: Measurements, modeling, and implications
809 for altimetry, *J. Geophys. Res. Earth Surf.*, 119(2), 349–365, doi:10.1002/2013JF002898, 2014.

810 Mosley-Thompson, E., McConnell, J. R., Bales, R. C., Li, Z., Lin, P.-N., Steffen, K., Thompson, L. G.,
811 Edwards, R. and Bathke, D.: Local to regional-scale variability of annual net accumulation on the Greenland
812 ice sheet from PARCA cores, *J. Geophys. Res.*, 106(D24), 33839, doi:10.1029/2001JD900067, 2001.

813 Mouginit, J., Rignot, E., Bjørk, A. A., van den Broeke, M., Millan, R., Morlighem, M., Noël, B., Scheuchl,
814 B. and Wood, M.: Forty-six years of Greenland Ice Sheet mass balance from 1972 to 2018, *Proc. Natl. Acad.*
815 *Sci.*, 201904242, doi:10.1073/pnas.1904242116, 2019.

816 Nghiem, S. V., Steffen, K., Neumann, G. and Huf, R.: Mapping of ice layer extent and snow accumulation
817 in the percolation zone of the Greenland ice sheet, *J. Geophys. Res. Earth Surf.*, 110(2), 1–13,
818 doi:10.1029/2004JF000234, 2005.

819 Nghiem, S. V., Hall, D. K., Mote, T. L., Tedesco, M., Albert, M. R., Keegan, K. M., Shuman, C. A.,
820 DiGirolamo, N. E. and Neumann, G.: The extreme melt across the Greenland ice sheet in 2012, *Geophys.*
821 *Res. Lett.*, 39(20), 6–11, doi:10.1029/2012GL053611, 2012.

822 Noël, B., van de Berg, W. J., Van Wessem, J. M., Van Meijgaard, E., Van As, Di., Lenaerts, J. T. M.,
823 Lhermitte, S., Munneke, P. K., Smeets, C. J. P. P., Van Uft, L. H., Van De Wal, R. S. W. and Van Den
824 Broeke, M. R.: Modelling the climate and surface mass balance of polar ice sheets using RACMO2 - Part 1:
825 Greenland (1958-2016), *Cryosphere*, 12(3), 811–831, doi:10.5194/tc-12-811-2018, 2018.

826 Nye, J. F.: Correction factor for accumulation measured by the thickness of the annual layers in an ice sheet,
827 *J. Glaciol.*, 4(36), 785–788, 1963.

828 Osterberg, E. C., Handley, M. J., Sneed, S. B., Mayewski, P. A. and Kreutz, K. J.: Continuous ice core melter
829 system with discrete sampling for major ion, trace element, and stable isotope analyses, *Environ. Sci.*
830 *Technol.*, 40(10), 3355–3361, doi:10.1021/es052536w, 2006.

831 Osterberg, E. C., Hawley, R. L., Wong, G. J., Kopec, B., Ferris, D. and Howley, J.: Coastal ice-core record
832 of recent northwest Greenland temperature and sea-ice concentration, *J. Glaciol.*, 61(230), 1137–1146,
833 doi:10.3189/2015JoG15J054, 2015.

834 Overly, T. B., Hawley, R. L., Helm, V., Morris, E. M. and Chaudhary, R. N.: Greenland annual accumulation
835 along the EGIG line, 1959–2004, from ASIRAS airborne radar and neutron-probe density measurements,
836 *Cryosph.*, 10(4), 1679–1694, doi:10.5194/tc-10-1679-2016, 2016.

837 Rennermalm, A. K., Moustafa, S. E., Mioduszewski, J., Chu, V. W., Forster, R. R., Hagedorn, B., Harper, J.
838 T., Mote, T. L., Robinson, D. A., Shuman, C. A., Smith, L. C. and Tedesco, M.: Understanding Greenland
839 ice sheet hydrology using an integrated multi-scale approach, *Environ. Res. Lett.*, 8(1), 015017,
840 doi:10.1088/1748-9326/8/1/015017, 2013.

841 Rodriguez-Morales, F., Gogineni, S. P., Leuschen, C. J., Paden, J. D., Li, J., Lewis, C. C., Panzer, B., Gomez-
842 Garcia Alvestegui, D., Patel, A., Byers, K., Crowe, R., Player, K., Hale, R. D., Arnold, E. J., Smith, L.,
843 Gifford, C. M., Braaten, D. and Panton, C.: Advanced multifrequency radar instrumentation for polar
844 Research, *IEEE Trans. Geosci. Remote Sens.*, 52(5), 2824–2842, doi:10.1109/TGRS.2013.2266415, 2014.

845 Sasgen, I., van den Broeke, M. R., Bamber, J. L., Rignot, E. J., Sorensen, L. S., Wouters, B., Martinec, Z.,
846 Velicogna, I. and Simonsen, S. B.: Timing and origin of recent regional ice-mass loss in Greenland, *Earth
847 Planet. Sci. Lett.*, 333–334, 293–303, doi:10.1016/j.epsl.2012.03.033, 2012.

848 Selesnick, I. W. and Sidney Burrus, C.: Generalized digital butterworth filter design, *IEEE Trans. Signal
849 Process.*, 46(6), 1688–1694, doi:10.1109/78.678493, 1998.

850 Serreze, M.: Northern Hemisphere cyclone locations and characteristics from NCEP/NCAR reanalysis data,
851 Verison 1, Natl. Snow Ice Data Center, Boulder, CO, Digit. media.[Available online [http://nsidc.
852 org/data/nsidc-0423.html](http://nsidc.org/data/nsidc-0423.html).], 2009.

853 Spikes, V. B., Hamilton, G. S., Arcone, S. A., Kaspari, S. and Mayewski, P. A.: Variability in accumulation
854 rates from GPR profiling on the West Antarctic plateau, *Ann. Glaciol.*, 39, 238–244,
855 doi:10.3189/172756404781814393, 2004.

856 Trusel, L. D., Das, S. B., Osman, M. B., Evans, M. J., Smith, B. E., Fettweis, X., McConnell, J. R., Noël, B.
857 and van den Broeke, M. R.: Nonlinear rise in Greenland runoff in response to post-industrial Arctic warming,
858 *Nature*, 564(7734), 104–108, doi:10.1038/s41586-018-0752-4, 2018.

859 Vandecrux, B., Fausto, R. S., Langen, P. L., Van As, D., MacFerrin, M., Colgan, W., Ingeman-Nielsen, T.,
860 Steffen, K., Jensen, N. S., Møller, M. T. and Box, J. E.: Drivers of Firn Density on the Greenland Ice Sheet
861 Revealed by Weather Station Observations and Modelling, *J. Geophys. Res. Earth Surf.*,
862 doi:10.1029/2017JF004597, 2018.

863 Vernon, C. L., Bamber, J. L., Box, J. E., Van Den Broeke, M. R., Fettweis, X., Hanna, E. and Huybrechts,
864 P.: Surface mass balance model intercomparison for the Greenland ice sheet, *Cryosph.*, 7(5), 599–614,
865 doi:10.5194/tc-7-599-2013, 2013.

866 Wong, G. J., Hawley, R. L., Lutz, E. R. and Osterberg, E. C.: Trace-element and physical response to melt
867 percolation in Summit (Greenland) snow, *Ann. Glaciol.*, 54(63), 52–62, doi:10.3189/2013aog63a602, 2013.

868 Wong, G. J., Osterberg, E. C., Hawley, R. L., Courville, Z. R., Ferris, D. G. and Howley, J.: Coast-to-interior
869 gradient in recent northwest Greenland precipitation trends (1952 – 2012), *Environ. Res. Lett.*, 10(11),
870 114008, doi:10.1088/1748-9326/10/11/114008, 2015.

871 Yilmaz, Ö.: *Seismic Data Analysis*, Society of Exploration Geophysicists., 2001.

872 Zumberge, J. F., Heflin, M. B., Jefferson, D. C., Watkins, M. M. and Webb, F. H.: Precise point positioning
873 for the efficient and robust analysis of GPS data from large networks, *J. Geophys. Res. Solid Earth*, 102(B3),
874 5005–5017, doi:10.1029/96JB03860, 1997.

875